Quantification of Turbulent Heat Fluxes and the Energy Balance Closure over a Flux Tower in the Semi-arid Savannah area of Naivasha, Kenya

JOHN MBATHA MUTINDA

February, 2017

SUPERVISORS:
Dr. Ir. Christiaan Van der Tol
Drs. Robert Becht

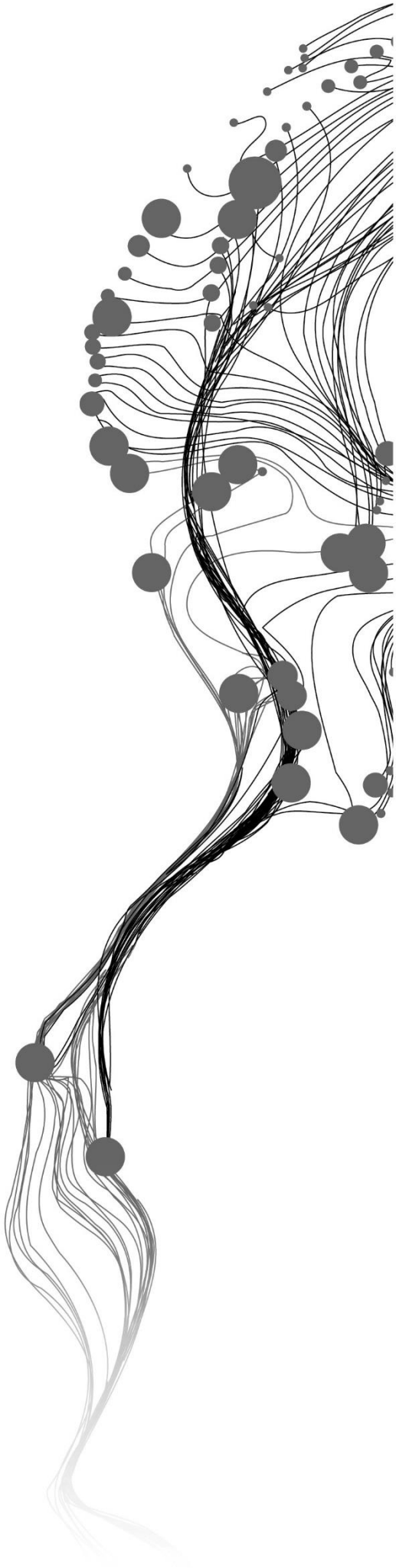

Quantification of Turbulent Heat Fluxes and the Energy Balance Closure over a Flux Tower in the Semi-arid Savannah area of Naivasha, Kenya

JOHN MBATHA MUTINDA
Enschede, The Netherlands, February, 2017

Thesis submitted to the Faculty of Geo-Information Science and Earth Observation of the University of Twente in partial fulfilment of the requirements for the degree of Master of Science in Geo-information Science and Earth Observation.
Specialization: Water Resources and Environmental Management.

SUPERVISORS:
Dr. Ir. Christiaan Van der Tol
Drs. Robert Becht

THESIS ASSESSMENT BOARD:
Prof. Dr. Z. Su (Chair)
Prof. Dr. U. Rascher (External Examiner, Cluster of Excellence in Plant Sciences, Julich, Germany)

ABSTRACT

Quantification of turbulent heat fluxes is important as they influence regional and global climates. This becomes very vital in semi-arid ecosystems where evapotranspiration accounts for ~90% of rainfall losses. The dependability of quantified fluxes as inputs into climate and hydrological models is hinged on energy balance closure and therefore it is important to quantify and understand sources of lack of energy balance closure; which remains to be an unresolved problem with many eddy covariance systems.

In this study, half hourly turbulent heat fluxes are derived using measurements from a flux tower situated in a semi-arid savannah area of Naivasha, Kenya, between the year 2012 and 2014, and over a brief period in 2016. Given that this site is not a full eddy covariance system owing to lack of a gas analyzer, latent heat fluxes are derived by inversion of the Bowen ratio derived from relative humidity and temperature measurements. In combination with ground heat flux estimated from a soil heat flux plate and soil temperature profile measurements; the energy balance closure is computed. Causes of lack of energy balance closure are evaluated, specifically the effects of quality filtering based on friction velocity, effects of flux footprint, effects of Bowen ratio inter-calibration and accuracy in ground heat flux estimation. Representativeness of tower measured net radiation is also evaluated by comparing it with net radiation retrieved from Landsat 8 OLI & TIRS satellite.

The overall energy balance ratio (EBR) for three years analysed (2012-2014) was 58% , while yearly EBR's were 67% for 2012, 56% for 2013, 51% for 2014 and 49% for 2 months analysed in 2016. Quality filtering of fluxes when u^* is less than 0.3 m s^{-1} improved the overall EBR for the three years evaluated by 5%. Filtering fluxes emanating from a road surface towards the east of the tower when wind direction is between 60˚- 120˚ improved the overall EBR further by 6%. Net radiation measured by the tower radiometer is found to be higher than net radiation retrieved from the satellite both at the tower pixel and when averaged over the tower source area. Correcting for the bias in net radiation improved the overall EBR by 5%. Combining filtering data when $u^* < 0.3$ m s^{-1}, when wind direction is between 60˚- 120˚ and correcting for bias in net radiation improved the overall EBR for three years (2012 – 2014) to 76% which is an 18% increase. Yearly EBRs increased to 83%, 77% and 69% for 2012, 2013 and 2014 respectively.

It is recommended that other possible factors attributed to lack of closure such as advection and averaging time that were not analysed in this study be evaluated. Further, it is recommended that a gas analyzer be added to the tower for more accurate measurements of latent heat fluxes.

Keywords: Energy Balance Closure, Flux Tower, Turbulent Heat Fluxes, Sensible Heat Flux, Latent Heat Flux, Ground Heat Flux, Energy Balance Ratio, Bowen Ratio, Inter-Calibration.

DEDICATION

This work is dedicated to my dear mother Cecilia Kaluki, who sacrificed a lot and fought to ensure that I had the best education.

ACKNOWLEDGEMENTS

First, I thank God for the opportunity to pursue an MSc. and for granting me good health during the entire period that I undertook this study. Secondly I would like to sincerely thank the Netherlands government for the funding.

I would also like to express a lot of gratitude to my family. Thank you for understanding that I had to be away from you, for your prayers and support. To my friend Wairimu, I will remain indebted to you for your sacrifice, understanding and support.

To my first supervisor Dr. Christiaan Van der Tol; thank you for sharing your knowledge with me. Despite your busy schedule; you always had time for me even when I showed up at your door without an appointment. You in a humble way introduced me to research basics; and from you I learnt Integrity. I will always be grateful for the opportunity I had to work with you. To Drs. Robert Becht and Dr. Joost Hoedjes; thank you for your incredible support during my fieldwork in Naivasha and for all your comments and inputs. To Ing. Murat Ucer, without your commitment in ensuring that I had all the equipment I needed, this study would not be possible. Thank you very much. To Dr. Vincent Odongo; in the words of Sir Isaac Newton, I have done this because I stood on your shoulders. I can never be able to repay you for providing me with the data that I used in this study, for your friendship, comments, and constructive criticism. Thank you for teaching me hard work; and for culturing a scientific mind in me. To Donald Rwasoka, the discussions that we had were of great help and are greatly appreciated.

I would also like to thank the Water Resources and Management authority, Naivasha for their support during my field work. To Dominic Wambua and Henry Munyaka thank you specially for your support.

Special thanks to Sammy Njuki and Amos Tabalia for encouraging me to join you in ITC. I do not regret it. To Muiruri Peter, thank you for your friendship and support.

To all my classmates and my colleagues Daniel, Fredrick, Kennedy, Calisto, Patrick, Loise, Nicholas, Petulo, Benson, Onyimbi, Grachen and Elizabeth with whom we walked this journey together; it is done. Thank you for standing by me.

Lastly, to the Kenyan community at ITC, your support and encouragement is greatly appreciated.

TABLE OF CONTENTS

LIST OF FIGURES

LIST OF TABLES

LIST OF ABBREVIATIONS

AFs	Atmospheric transfer Functions
AMMA	African Monsoon Multi-disciplinary Analysis
DN	Digital Number
DOS	Dark Object Subtraction
EBR	Energy Balance Ratio
ECMWF	European Centre for Medium-Range Weather Forecasts
ENVI	ENvironment For Visualizing Images
ET	Evapotranspiration
ETM	Enhanced Thematic Mapper
FFP	Flux Footprint Prediction
FVC	Fractional Vegetation Cover
HAPEX	Hydrology Atmosphere Pilot Experiment
ILWIS	Integrated Land and Water Information System
KWSTI	Kenya Wildlife Service Training Institute
LE	Latent Heat
LSE	Land Surface Emissivity
LST	Land Surface Temperature
MATLAB	Matrix Laboratory
MODIS	Moderate Resolution Imaging Spectroradiometer
NDVI	Normalized Difference Vegetation Index
NIR	Near Infrared
OLI	Operational Land Imager
QGIS	Quantum Geographic Information System
RH	Relative Humidity
RHT	Relative Humidity and Temperature
RMSE	Root Mean Square Error
TIGR61	TOVS Initial Guess Retrieval
TIRS	Thermal Infrared Sensor
TOA	Top of the Atmosphere
USGS	United States Geological Survey
VIS	Visible
WRMA	Water Resources Management Authority

1. INTRODUCTION

1.1. Background

Turbulent fluxes transport gases, energy and other substances in the atmospheric boundary layer at different scales both spatially and temporally (Zhang et al., 2014). In order to understand surface atmosphere interactions, it is important to quantify and partition turbulent fluxes since they influence local, regional and global climates making them crucial in eco-hydrological, weather and climate studies (Dirmeyer, 1994). In arid and semi-arid regions particularly, 90% of annual precipitation is lost as evapotranspiration (ET) (Huxman et al., 2005), making latent heat (LE) a major component of the energy balance. Quantification of turbulent fluxes and the energy balance for such ecosystems is thus important (Odongo et al., 2016).

Several methods have been developed for flux quantifications, amongst them the Bowen ratio method, the aerodynamic gradient method and the eddy covariance method. The Bowen ratio and Aerodynamic gradient are indirect methods and involve measurements at two heights. Though they use simple equipment, they may not be able to measure very small gradients in temperature. The eddy covariance method on the other hand is a direct method that involves measurement at one height (Moncrieff et al. (1997).

Eddy covariance measurement systems are currently the most preferred for quantification of turbulent fluxes, following their development over the last two decades, especially because such systems can also be used to quantify CO_2 fluxes (Evans et al., 2012). These systems have however been associated with the problem of energy imbalance as discussed by Foken et al. (2006); and to increase the dependability of fluxes measured by eddy covariance systems, it is important to determine and understand the source of these imbalances (Twine et al., 2000).

This study is therefore aimed at quantifying turbulent fluxes and analyzing the energy balance using flux measurements taken by an eddy covariance system installed in a semi-arid savannah area of Naivasha, Kenya, with a specific focus of investigating the sources of lack of energy balance closure. This site relies on Bowen ratio method for estimation of Latent heat fluxes as a gas analyzer is not permanently installed, apart from a 40 day period during the year 2012.

1.2. Problem Statement

The number of measurements of energy fluxes in heterogeneous savannah ecosystems is limited (Kurc & Small, 2004). In the case of East Africa particularly, these limitations are aggravated by lack of adequate instrumentation for long term measurements and studies. For the first time in this region, long term flux measurements are now available through a flux tower installed at the Naivasha savannah in Kenya, which has been recording micro-meteorological and flux measurements since the year 2012. Odongo et al. (2016) presents the first analysis of energy fluxes using measurements from this tower. With 3 year data recorded between the years 2012 and 2014, they report an energy balance ratio of 0.65. A detailed analysis to determine the source of low closure has however not been carried out. Lack of energy balance closure in eddy covariance measurement systems has been reported in many studies. Errors of 10-30% are common (Sánchez, Caselles, & Rubio, 2010). Such energy imbalance has an impact on the interpretation and

application of the measured fluxes and how they compare to modelled estimates. It is therefore important to determine, understand and explain the source of this low closure (Twine et al., 2000).

1.3. Objectives

1.3.1. Main Objectives

To quantify turbulent heat fluxes and analyze the causes of the energy balance closure error using measurements taken by a flux tower in the semi-arid savannah area of Naivasha, Kenya; between 2012 and 2014.

1.3.2. Specific Objectives

1. To determine the energy balance closure.
2. To determine the effects of quality filtering of data for underdeveloped turbulence based on friction velocity.
3. To investigate whether the flux footprint extends into the nearby urban area, and the effect of this on energy balance closure.
4. To investigate the effect of errors in Bowen ratio measurements on the energy balance closure.
5. To investigate the measurement accuracy of ground heat flux, the representativeness of net radiation and its effect on the energy balance closure.

1.3.3. Research Questions

1. What is the energy balance closure of flux measurements taken between 2012 and 2014?
2. What is the effect of filtering data for underdeveloped turbulence based on friction velocity on the energy balance closure?
3. What is the effect of Bowen ratio measurement errors due to accuracy and precision of the temperature and relative humidity instruments on the energy balance closure?
4. Is there an error in the estimation of ground heat flux and how does this affect the energy balance closure?
5. How representative is net radiation measured by the tower radiometer in reference to the turbulent fluxes source area?

2. STUDY AREA

2.1. Study Area

The flux tower is located within the L. Naivasha basin in Kenya as shown in Figure 2.1. It is inside a protected area which hosts the Kenya Wildlife Service Training Institute (KWSTI).

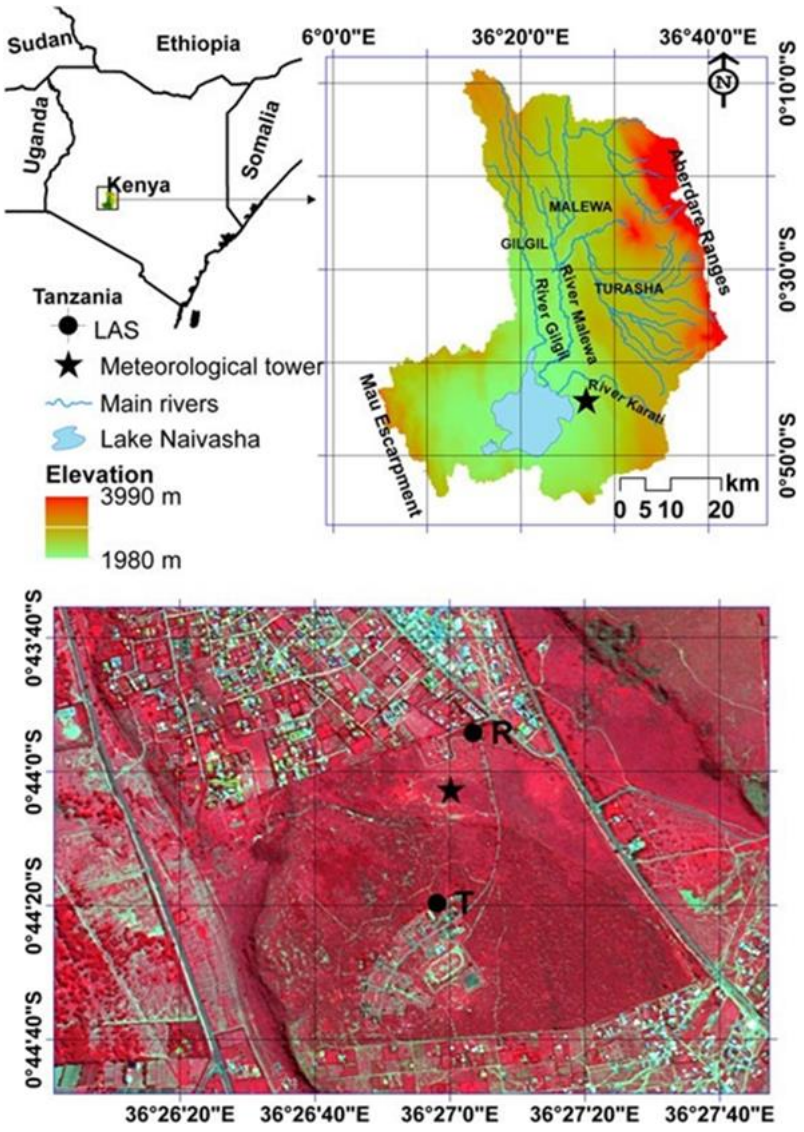

Figure 2.1: Location of flux tower. The tower is marked with a star. T and R refer to the transmitter and receiver of the scintillometer respectively (Odongo et al., 2016).

2.1.1. Climate and Vegetation

The study area is at an elevation of ~2000m above sea level. Lake Naivasha catchment in which the tower is located experiences two rainy seasons. Long rains occur between March and May, while short rains occur between October and December. The area receives an average rainfall of 610mm per annum. Vegetation of the area is characterized by shrubs and a few scattered trees with a grass cover of 40-60%. Shrubs exhibit a general height of 0.5-1m. Shrubs shed leaves and grass dries during the dry season, then

sprouting occurs shortly after the rains. The flux tower site is generally flat with a gentle slope towards the lake on the West. The terrain goes up towards the East. (Odongo et al., 2016).

2.1.2. Instrumentation

The flux tower has a height of 5.5 metres and is installed with the instruments described in Table 2.1. It has been operational since January 2012.

Table 2.1: Flux tower instrumentation (Odongo et al., 2016).

No.	Instrument description	Parameter
1.	3D sonic anemometer (WindMaster (Pro) type 1516, Gill Instruments Limited, Hampshire, UK). -Sampling frequency 10Hz	Wind velocity, Virtual temperature fluctuations
2.	HFM53, Rotronic Instruments (UK) Limited, West Sussex, UK)	Aspirated air temperature & relative humidity at 1.8m and 5.5m above ground level -Enables Bowen ratio computation
3.	NR101 four component radiometer (Hukseflux, Delft, The Netherlands) -At 2.5m above the ground	Downward and upward solar and long wave radiation
4.	10kΩ NTC (Campbel-107, Campbell Scientific Inc., Logan, UT, USA) -Installed at 1, 2, 3, 4, 5, 6, 7, 8, 10 and 12.5 cm depths below the ground	Soil temperature profiles
5.	Decagon EM50 5ET soil moisture sensors(Decagon Devices Inc., Washington, USA)	Soil water content
6.	Dielectric leaf wetness sensor (LWS-L Campbell Scientific Inc., Logan, UT, USA)	Dew presence
7.	Infra-red remote temperature sensor (IR100 Campbell Scientific Inc., Logan, UT, USA)	Surface temperature
8.	Soil Heat Flux Plate (HFP01SC, Hukseflux, Delft, The Nether- lands) -Installed at 10cm depth below the ground	Soil heat fluxes
9.	Tipping bucket rain gauge (Rain Collector II, Davis Instruments, USA)	Rainfall

All the instruments are connected to a CR3000 data logger (Campbell Scientific Inc., Logan, UT, USA); apart from soil moisture sensors which are connected to a separate data logger. Soil heat fluxes are recorded at intervals of 15 minutes, soil water content at 30 minutes and other hydro-meteorological variables at 1 minute. A gas analyzer (LI-7500, Li-COR Biosciences, Nebraska, USA) was introduced between 21/03/2012 and 9/05/2012. It was installed at 5.5m above the ground and recorded at 10Hz. A large aperture scintillometer (Scintec BLS 450) with a propagation length of 810m was also installed at 6.85 metre path height above the ground. It operated between 7/02/2012 and 4/12/2012, but it did not take continuous measurements due to intermittent failures. Figure 2.2 shows some of the flux tower instrumentation and views of the immediate vicinity in different directions.

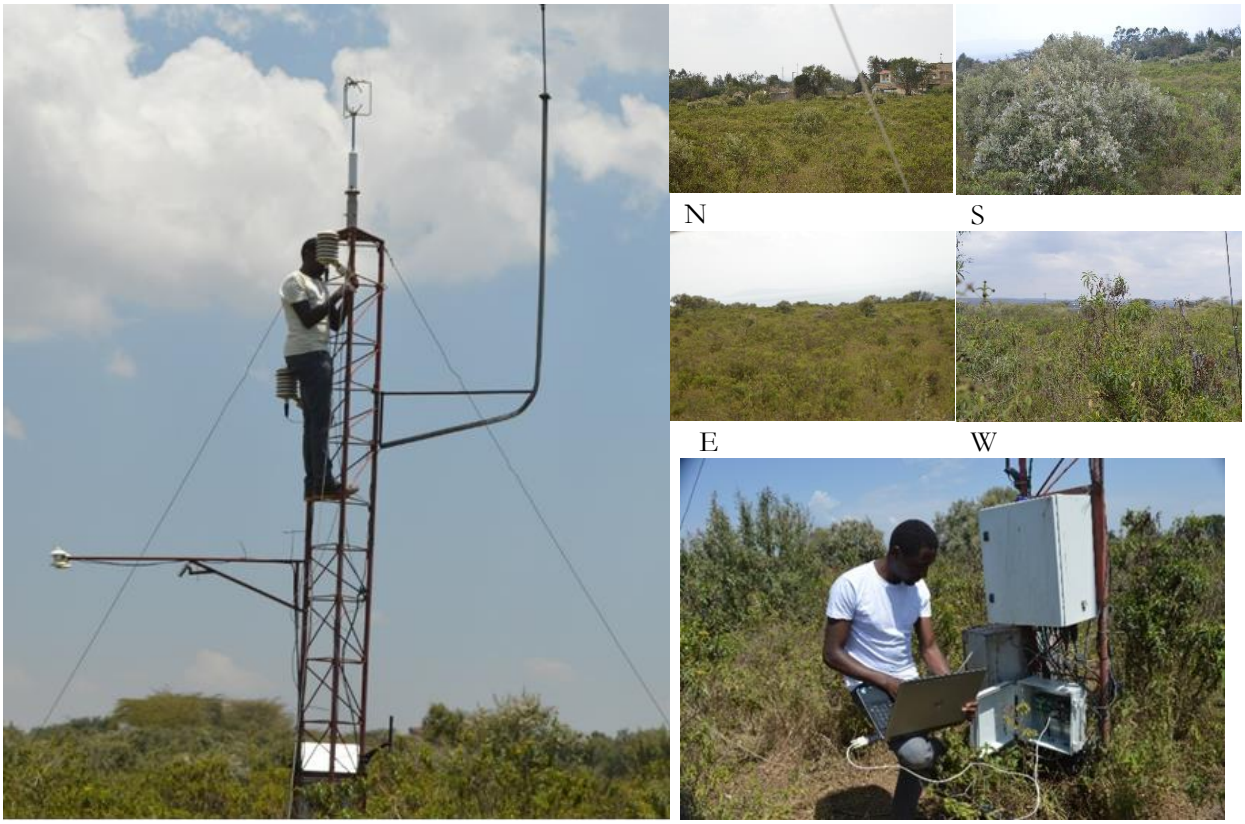

Figure 2.2: Photograph of Naivasha flux tower taken on 23/9/2016 showing different instrumentations and views in different directions.

2.1.3. Field Work and Data Collection

Field work was conducted between September 13th and October 4th 2016. Site visits, data acquisition and inspection of the general condition of the tower instrumentation was done during this period. Data for inter-calibration of the Bowen ratio measuring instruments was acquired by mounting the two set of Relative Humidity and Temperature (RHT) sensors at the same height and taking measurements for 5 days. In addition to the already existing soil heat flux plate, four soil heat flux plates (HFP01SC, Hukseflux, Delft, The Netherlands) were installed radially around the tower in the NW, SW, NE and SE directions, each at a depths of 5cm. The flux plates were connected to a separate CR1000 data logger and recorded measurements at 10 minute intervals. Long term flux measurements from the year 2012 to 2014 were obtained from Vincent Odongo. A summary of the data used for this study is shown in Table 2.2.

Table 2.2: Summary of data sets

No.	Data Set	Source
1.	Flux tower measurements	Data loggers on site, Vincent Odongo.
2.	Landsat 8 OLI & TIRS images	Downloaded from http://earthexplorer.usgs.gov/
3.	Bowen ratio inter-calibration measurements	Field work: Mounting the humidity and temperature sensors at same level and taking measurements for 2 days
4.	Ground heat flux validation measurements	Field work

2.1.4. Satellite Data

Landsat 8 Operational Land Imager (OLI) and Thermal Infrared Sensor (TIRS) images were downloaded from http://earthexplorer.usgs.gov/ using QGIS, an open source software. A total of 11 images (path 169 and row 60), with cloud cover less than 10% for the period between July 2013 and December 2014 were downloaded. Landsat 8 OLI and TIRS images consist of 9 bands with a spatial resolution of 30 metres for band 1 to 7 and band 9. Thermal bands 10 and 11 are collected at 100metres but resampled to 30 metres (USGS, 2016). The panchromatic band (band 8) is at 15metres resolution. Landsat 8 was launched in February 11th 2013 and it reached operational orbit on April 11th 2013. Table 2.3 shows a summary of description of Landsat 8 bands and their wavelength ranges.

Table 2.3: Description of Landsat 8 OLI and TIRS bands (USGS, 2016).

Band	**Wavelength [µm]**
Band 1 - Coastal aerosol	0.43 – 0.45
Band 2 - Blue	0.45 – 0.51
Band 3 - Green	0.53 – 0.59
Band 4 - Red	0.64 – 0.67
Band 5 - Near Infrared(NIR)	0.85 – 0.88
Band 6 - SWIR 1	1.57 – 1.65
Band 7 - SWIR 2	2.11 – 2.29
Band 8 - Panchromatic	0.50 – 0.68
Band 9 - Cirrus	1.36 – 1.38
Band 10 - Thermal Infrared (TIRS) 1	10.60 – 11.19
Band 11 - Thermal Infrared (TIRS) 2	11.50 – 12.51

3. THEORETICAL BACKGROUND

Turbulent heat fluxes between the land and the atmosphere influence weather and climate processes at global, regional and local scales, and it is therefore important to understand the processes by which the flux exchanges occur. In arid and semi-arid ecosystems, about 90% of annual precipitation is lost as ET making quantification and partitioning of turbulent heat fluxes vital for the hydrology of such areas (Odongo et al., 2016).

In the past, methods such as the aerodynamic gradient and the Bowen ratio have been used to study fluxes. With the development of sonic anemometers, the eddy covariance method has become a preferred method of quantifying turbulent fluxes (Moncrieff et al., 1997).

The first coordinated eddy covariance systems were by EUROFLUX as detailed by Aubinet et al. (1999) followed by AMERIFLUX. Success of the two led to implementation of the FLUXNET, a global system of eddy covariance towers mostly over Europe, North and South America, parts of Asia, and a few locations in Africa (Baldocchi et al., 2001).

In Africa, several studies have been conducted, amongst them the African Monsoon Multidisciplinary Analysis (AMMA) extensively described by Redelsperger et al., (2006) and the HAPEX-Sahel (Goutorbe et al., 1997). Measurements over East Africa are however very limited due to lack of proper instrumentation for long term measurements. Odongo et al. (2016) presented the first known 'long term' (i.e., multiple-years) flux measurements in this region through a flux tower installed in the semi-arid savannah area of Naivasha, Kenya

3.1. The Energy Balance Closure Problem

Energy balance is closed when the energy incoming into a system equals the energy outgoing plus any change in energy storage in the system. This is expressed as:

$$R_n = G + H + LE + C \qquad 3.1$$

where R_n is the net radiation, G is the ground heat flux, H is the sensible heat flux, LE is the latent heat flux and C is the closure or residual term. Following the principle of energy conservation (first law of thermodynamics), the energy balance residual term should be zero (M. Aubinet et al., 1999). However, with many eddy covariance systems, this is not the case. Many studies have reported imbalances of 10-30% (Twine et al., 2000). The problem of lack of energy closure continues to be unresolved and many researchers have tried to evaluate the source of these imbalances. Different studies attribute lack of energy balance closure to: (i)systematic measurement errors, (ii)neglected energy storages, (iii)mismatch in the footprints of turbulent fluxes and the available energy, (iv) advection, and (v)losses through uncaptured high or low frequency contributions to turbulent fluxes (Kidston et al., 2010).

3.1.1. Systematic Measurement Errors

Instrument uncertainty is difficult to quantify given that it is often fused with other multiple factors and thus difficult to single out. Using pairs of instruments from collocated towers, Dragoni et al. (2007) estimated instrument uncertainty of ~ 13%. As discussed by Baldocchi et al. (2001), FLUXNET emphasizes the importance of instrument calibration as this can reduce measurement errors. To minimize errors, regular instrument calibration to account for instrument drifts need to be done (Aubinet, Vesala, & Papale, 2012).

3.1.2. Neglected Energy Storages

Including energy storage within the canopy is important when analyzing closures over forests and densely vegetated areas. Wilson et al., (2002) found that including canopy storage improved closure by up to 7% in FLUXNET sites within forests. Including canopy storage in sparsely vegetated areas does not significantly improve closure as this term is very small in such areas. For sparsely vegetated areas like grasslands and farmlands, including soil heat storage term (G) improved closure by up to 20%.

3.1.3. Mismatch in the Footprints of Turbulent Fluxes and the Available Energy

Net radiation and soil heat flux source areas are in order of few metres from the tower, while turbulent fluxes source areas can be hundreds of metres in the upwind direction and as such, there is always a mismatch. Having the turbulent fluxes being measured from a different surface than that of the residual energy measurements is an obvious source of lack of energy balance closure as discussed by Wilson et al. (2002).

3.1.4. Advection

One of the theoretical requirements for eddy covariance measurements is lack of advection. Horizontal advection can however be substantial, especially over heterogeneous areas (Vidale et al., (1997). Lee & Hu (2002) attributed lack of closure during nocturnal periods to advection

4. RESEARCH METHODOLOGY

4.1. Methodology Flowchart

Figure 4.1 shows a flowchart summarizing the methodology that was adopted in this study.

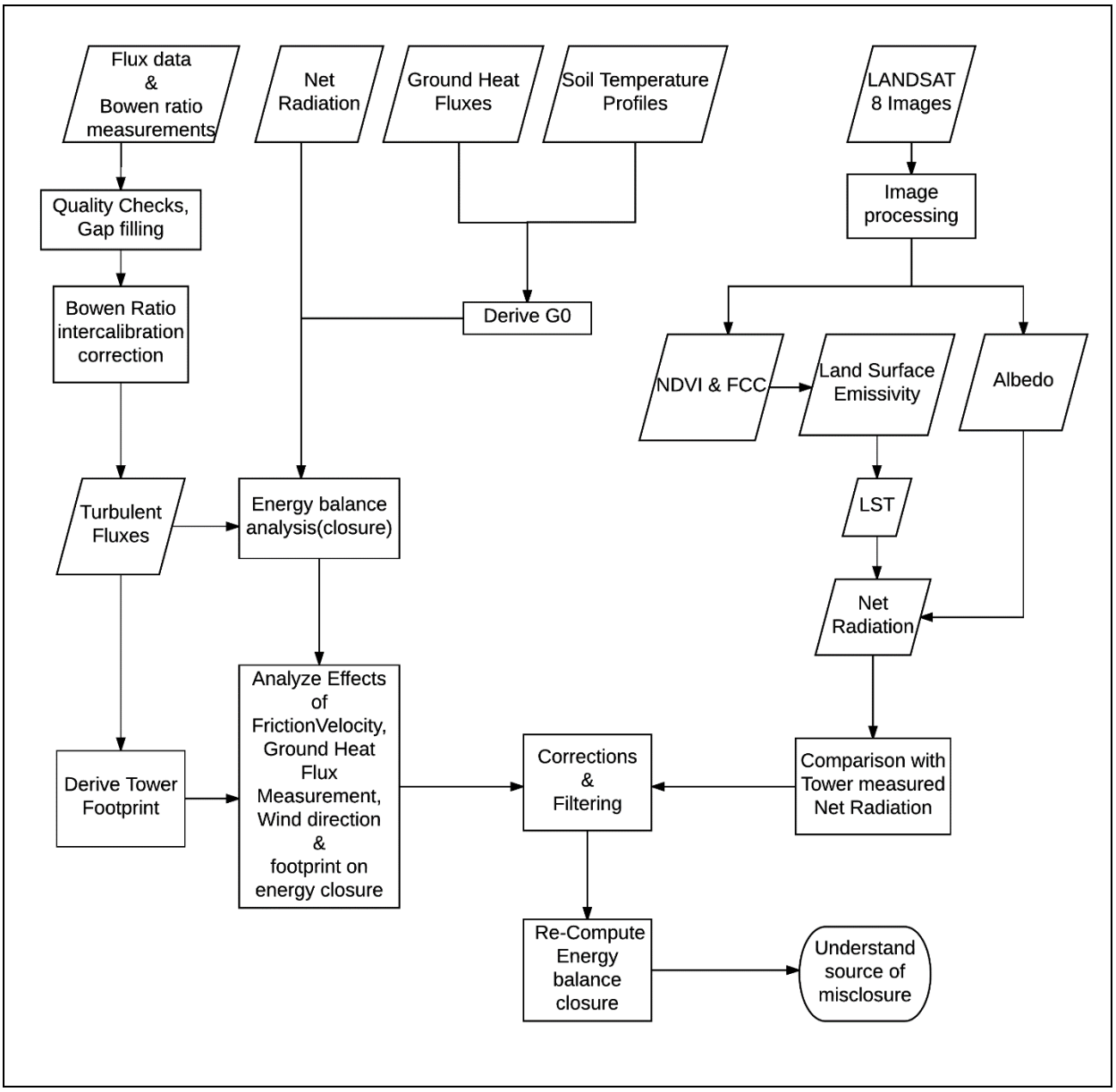

Figure 4.1: Methodology Flowchart

4.2. Data Quality Checks

Theoretical requirements for eddy covariance measurements include steady state conditions, fully developed turbulence and horizontal homogeneity. Procedures suggested by Foken et al. (2004) were used to check for fulfilment of steady state and turbulence requirements and data that did not fall within class 1

to 3 in the overall quality flagging classification was flagged out. These flags were implemented in Alteddy 3.9 software used to process turbulent fluxes.

4.3. Turbulent Fluxes

Half-hourly averaged turbulent fluxes were processed from the flux measurements using Alteddy software version 3.90 (http://www.climatexchange.nl/projects/alteddy/), developed by the Alterra Institute, Wageningen University, The Netherlands. Standard corrections applied during the flux data processing included angle of attack correction following Nakai (2006), 2D axis rotation (Finnigan, 2004), despiking (Vickers & Mart, 1997) and frequency response corrections (Moore, 1986).

Alteddy only processed latent heat fluxes over a short period of time (between 21/03/2012 and 09/05/2012) when the gas analyzer was operational. For the rest of the time series, only sensible heat fluxes were processed, and latent heat fluxes were derived using the Bowen ratio method. The Bowen ratio first proposed by Bowen (1926) is the ratio of sensible heat flux to water vapour flux; and is expressed as:

$$\beta = \frac{H}{LE} = \gamma \frac{\Delta T/\Delta Z}{\Delta e/\Delta Z} \quad 4.1$$

Where γ is the psychometric constant (kPa K^{-1}), $\Delta T/\Delta Z$ is the vertical temperature gradient and $\Delta e/\Delta Z$ is the vertical actual water vapour gradient. Temperature and relative humidity gradients are measured across two fixed heights. Saturated vapour pressure at the two heights was computed using Eq. 4.2 (Buck, 1981).

$$e_s = 6.1121 \exp\left(\left(18.678 - \frac{T}{234.5}\right)\left(\frac{T}{257.14 + T}\right)\right) \quad 4.2$$

Where e_s is the saturation vapour pressure (kPa) and T is temperature (°C). The relationship between saturated vapour pressure and relative humidity in Eq. 4.3 was used to calculate actual vapour pressure at the two heights enabling computation of Δe from relative humidity RH (expressed as percentage).

$$e = e_s * \frac{RH}{100} \quad 4.3$$

LE was then calculated by inverting the Bowen ratio as shown in Eq. 4.4

$$LE = \frac{H}{\beta} \quad 4.4$$

The Bowen ratio method yields unreasonable fluxes when $\beta \approx$ -1. This tends to occur during early morning hours, in the afternoon and during precipitation (Ohmura Atsumu, 1982). Fluxes during precipitation and when Bowen ratio approached -1, i.e. -1.25 < β < -0.75 were excluded (Payero et al., 2003).

4.4. Inter-calibration of Bowen ratio measuring equipment

As aforementioned, Bowen ratio is calculated using temperature and humidity gradients across two fixed heights. Given that the instruments have been in the field for a long time, there is a possibility of a slight drift which may result in systematic measurement errors (Tomlinson, 1996), thus the need for inter-calibration. Inter-calibration is based on the premise that measurements from two identical equipment under similar conditions should be equal (Tang & Li, 2014). To obtain inter-calibration data, both the Relative Humidity and Temperature (RHT) sensors were mounted at the same height and measurements taken for a period of 5 days, between 19th and 23rd September 2016. Equations used for inter-calibration correction were obtained by second order polynomial regression of RH_1 against RH_2, and linear regression of T_1 against T_2. RHT_2 was chosen as the reference, and the coefficients obtained from the regressions were used to correct RH_1 and T_1 measurements. Figure 4.2 shows regression plots of RHT measurements taken between 19th and 23rd September 2016 when the sensors were mounted at the same height.

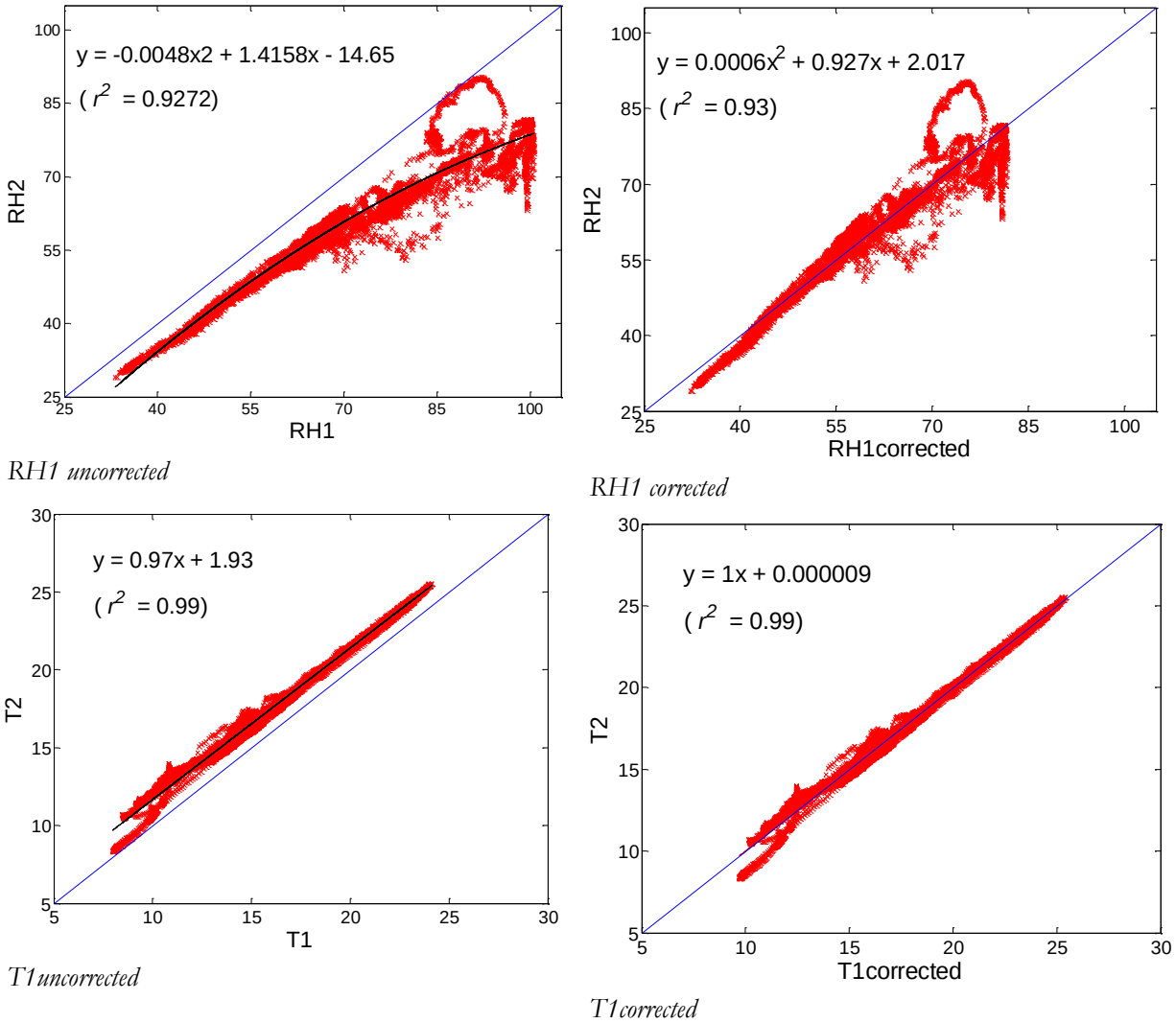

RH1 uncorrected

RH1 corrected

T1uncorrected

T1corrected

Figure 4.2: Regression plots used to obtain equations used for RH and T inter-calibration correction. The blue line indicates 1:1 relationship.

4.5. Ground Heat Flux

Ground heat flux often receives less attention in comparison with other components of the energy balance, since it is considered the smallest term. Heat absorbed during the day is emitted during the night, and therefore its summation over 24hrs is close to zero (C Van der Tol & Parodi, 2011). For instantaneous energy balance however, ground heat flux accounts for considerable percentage especially in sparsely vegetated areas and savannahs, and as such it cannot be neglected. Ground heat flux at midday for example can range from 30-45% for dense vegetation and bare soil respectively (Heusinkveld et al., (2004); Clothier et al., (1986).

In this study, ground heat flux at the surface was derived using the procedures of Christiaan van der Tol, (2012); which rely on the heat diffusion equation (Eq. 4.5) and the continuity equation for transfer of heat vertically (Eq. 4.6).

$$G(z,t) = -\lambda_s \frac{\partial T(z,t)}{\partial z} \quad 4.5$$

$$c_v \frac{\partial T(z,t)}{\partial t} = -\frac{\partial G(z,t)}{\partial z} \quad 4.6$$

Where λ_s is the thermal conductivity of soil (J m^{-1} s^{-1} K^{-1}); T is the soil temperature (°C or K), z is the soil depth (m) and c_v is the volumetric heat capacity (J m^{-1} s^{-1} K^{-1}). Combining equation 4.5 and 4.6 gives the thermal diffusion equation (4.7).

$$\frac{\partial \mathrm{T}}{\partial t} = D \frac{\partial^2 T}{\partial z^2} \quad 4.7$$

Where $D = \lambda_s / c_v$ is the soil heat diffusivity (m^2 s^{-1}). Given that soil heat flux has a periodic nature caused by solar radiation, sinusoidal functions are chosen as boundary conditions to Eq. 4.7. Solving the periodic boundary condition yields eq. 4.8:

$$T(z,t) = \sum_{k=0}^{n} A_k \sin(\omega k t - Kz) + B_k \cos(\omega k t - Kz)) \exp(-Kz) \quad 4.8$$

With this equation, temperature time series at any depth can be simulated analytically. Using Eq. 4.8 in Eq. 4.5 yields an equation for ground heat flux at the surface as a function of temperature:

$$G_0(t) = \Gamma \sum_{k=0}^{n} \sqrt{k\omega/2}\,((A_k - B_k)\sin(\omega k t) + (A_k + B_k)\cos(\omega k t)) \quad 4.9$$

Where $\Gamma = c_v . \sqrt{D}$ is the thermal inertia of soil (J m^{-2} K^{-1} s$^{-1/2}$). Diffusivity was estimated by calibration of Eq. 4.8 to a measured temperature profile using the least square algorithm 'lsqnonlin' in MATLAB. Using an initial value of D, temperature time series at all depths is simulated and the squared difference between the measured and simulated temperature is used as objective function for minimisation following procedures by Christiaan van der Tol (2012) . All the analysis were done using MATLAB R2013b.

4.6. Energy Balance Closure

Energy balance closure was evaluated using two methods as discussed by Wilson et al. (2002). One method involves linear regression of the sum of the turbulent fluxes ($H + LE$) against the residual energy ($R_n - G$). The slope and intercept (linear regression coefficients) quantifies the closure. A slope of one and an intercept of zero implies ideal closure. Another method for analysing closure is the Energy balance Ratio (EBR) which involves dividing the sum of turbulent fluxes with the sum of the residual energy as shown in Eq. 4.10.

$$\text{EBR} = \frac{\sum(H + LE)}{\sum(R_n - \text{G})} \quad 4.10$$

The advantage of EBR method is that it averages half hourly periods random errors over longer timescales.

4.7. Satellite Data Processing

4.7.1. Atmospheric correction

Atmospheric correction of satellite images was done using Dark Object Subtraction (DOS1) using QGIS software. The location of the study area near a deep water body (L. Naivasha) makes this method suitable. As described by Song et al. (2001), DOS1 method assumes existence of a dark object within the image, which has very low DN values. It is assumed that the minimum DN value is due to an atmospheric effect, and thus it is subtracted from all the pixels. Thermal bands (band 10 and 11) were corrected using the thermal atmospheric correction tool in ENVI software.

4.7.2. DN Conversion to TOA Reflectance and Radiance

Conversion from DN to TOA reflectance for VIS/NIR and radiance for TIR bands was done using equations 4.11, 4.12 and 4.13 as outlined in USGS (2016).

$$L_\lambda = M_L Q_{CAL} + A_L \quad 4.11$$

Where L_λ is the TOA spectral radiance (W m^{-2} $srad^{-1}$ μm^{-1})), M_L is the band specific radiance multiplicative factor, Q_{CAL} is the DN number and A_L is the band specific radiance additive rescaling factor.

$$\rho\lambda' = M_\rho Q_{CAL} + A_\rho \quad 4.12$$

$$\rho\lambda = \frac{\rho\lambda'}{cos(\theta_{SZ})} \quad 4.13$$

Where $\rho\lambda'$ is the TOA planetary reflectance without sun angle correction, $M\rho$ is the band specific reflectance rescaling factor, $A\rho$ is the reflectance additive rescaling factor $\rho\lambda$ is the TOA planetary reflectance corrected for sun angle and θ_{SZ} is the local solar zenith angle. Rescaling factors and solar zenith angle were obtained from the image metadata files.

4.7.3. Normalized Difference Vegetation Index (NDVI)

NDVI maps were derived from band 4 and band 5 (red and near-infrared bands) of atmospherically corrected images using equation 4.14

$$\mathrm{NDVI} = \frac{\rho_5 - \rho_4}{\rho_5 + \rho_4} \quad 4.14$$

Where ρ_5 and ρ_4 are land surface reflectances of band 5 and band 4 respectively.

4.7.4. Fractional Vegetation Cover (FCC)

Fractional vegetation cover (FVC) maps which are required for estimation of land surface emissivity were derived from NDVI using equation 4.15.

$$\mathrm{FVC} = \frac{NDVI - NDVI_S}{NDVI_V + NDVI_S} \quad 4.15$$

Where $NDVI_S$ and $NDVI_V$ refer to NDVI of soil and NDVI of vegetation respectively. The challenge with this method is determining the NDVI thresholds especially for soil which is characterized by more variation. For this study, $NDVI_S$ and $NDVI_V$ were chosen as 0.15 and 0.9 respectively as suggested by Jiménez-Muñoz et al. (2009). FVC was set to zero in pixels with $NDVI < NDVI_S$ and to one for pixels with $NDVI > NDVI_V$.

4.7.5. Land Surface Emissivity (LSE)

Land surface emissivity maps were calculated using simplified NDVI thresholds method proposed by (Sobrino et al. (2008), given by equation 4.16

$$\varepsilon = \begin{cases} \varepsilon_s & NDVI < NDVI_S \\ \varepsilon_s + (\varepsilon_v - \varepsilon_s) * \mathrm{FVC}, & NDVI_s \leq NDVI \leq NDVI_v \\ \varepsilon_v & NDVI > NDVI_V \end{cases} \quad 4.16$$

Where ε_s refers to emissivity of soil, and ε_v is the emissivity of vegetation. Yu, Guo, & Wu (2014) calculated Band 10 emissivity for Landsat 8 TIRS from University of California MODIS emissivity library and obtained values of 0.9668 and 0.9863 for soil and vegetation respectively. These values were adopted for this study.

4.7.1. Albedo

Total shortwave broadband albedo maps were derived using equation 4.17 first proposed by Liang et al. (2003) for Landsat 7 ETM+. The bands were shifted appropriately for its applicability in Landsat 8 OLI.

$$\alpha = 0.356_{\rho 2} + 0.130_{\rho 4} + 0.373_{\rho 5} + 0.085_{\rho 6} + 0.072_{\rho 7} - 0.0018 \quad 4.17$$

Where α is the shortwave broadband albedo, and ρi refers to spectral albedos.

4.7.2. Land Surface Temperature (LST)

USGS has raised concerns about stray light effect on Landsat 8 thermal bands, which is described in Landsat 8 data user handbook (USGS, 2016). They caution users against use of band 11 which appears to be more affected in land surface temperature retrieval algorithms such as the split window algorithm (USGS, 2015). In this study therefore, a generalised single channel algorithm first developed by Jiménez-Muñoz & Sobrino (2003) and revised by Jimenez-Munoz et al. (2009) was used. Only band 10 TIR data was utilised. The general formulation followed in single channel approach is as given in equations 4.18;

$$T_s = \gamma \left[\frac{1}{\varepsilon} (\varphi_1 L_{sen} + \varphi_2) + \varphi_3 \right] + \delta \quad 4.18$$

Where T_s is the land surface temperature (LST), L_{sen} is the at sensor radiance and ε is the surface emissivity. γ and δ are parameters dependent on the Planck's function calculated using equations 4.19 and 4.20.

$$\gamma \approx \frac{T_{sen}^2}{b_\gamma L_{sen}} \quad 4.19$$

$$\delta \approx T_{sen} - \frac{T_{sen}^2}{b_\gamma} \quad 4.20$$

Where T_{sen} is at sensor brightness temperature and the parameter b_γ is taken to be 1277K. These parameters are described in detail by Jimenez-Munoz et al. (2009). Parameters φ_1 , φ_2 and φ_3 represent atmospheric transfer functions (AF's), and are dependent on atmospheric transmissivity, which is determined by water vapour content in the TIR region. They are derived using a matrix notation in equation 4.21.

$$\begin{bmatrix}\varphi_1\\ \varphi_2\\ \varphi_3\end{bmatrix} = \begin{bmatrix}C_{11} & C_{12} & C_{13}\\ C_{21} & C_{22} & C_{23}\\ C_{31} & C_{32} & C_{33}\end{bmatrix}\begin{bmatrix}w^2\\ w\\ 1\end{bmatrix} \quad 4.21$$

Where w is the water vapour content and C_{ij} are coefficients obtained by simulation. In this study, coefficients in Table 4.1; obtained by Jimenez-Munoz et al., (2009) from the TIGR61 database were used.

Table 4.1: Coefficients from TIGR61 database for estimating atmospheric transfer functions (AF's)

C_{ij}	i = 1	i = 2	i = 3
j = 1	0.07593	-0.07132	1.08565
j = 2	-0.61438	-0.70916	-0.19379
j = 3	-0.02892	1.46051	-0.43199

Total column water vapour content estimates (w) were obtained from ECMWF. Retrieved water vapour values together with calculated AF's are shown in Table 4.2. Sample maps of LST derived using the single channel algorithm are shown in Appendix A.

4.7.3. Net Radiation

Net radiation maps were calculated using equation 4.22

$$R_n = (1 - \alpha)R_{si} + R_{li} - R_{lo} \quad 4.22$$

Where R_n is the net radiation, α is broadband shortwave albedo (from albedo maps), R_{si} is the incoming shortwave radiation, R_{li} is the incoming longwave radiation and R_{lo} is the outgoing longwave radiation. R_{lo} maps were calculated using equation 4.23.

$$R_{lo} = (1 - \varepsilon)R_{li} + \varepsilon\sigma T_0^4 \quad 4.23$$

Where σ is the Stefan Boltzmann constant (5.67×10^{-8} W m^{-2} K^{-1}), ε is the emissivity (from emissivity maps) and T_0 is the land surface temperature in Kelvin (from LST maps). Given that emissivity maps were

used for LST maps retrieval, any errors in the emissivity estimation are compensated for in the calculation of broadband outgoing albedo in eq. 4.23. R_{si} and R_{li} values were obtained from the ground measurements at the flux tower corresponding to the satellite overpass time. ILWIS software map calculation was extensively used in implementing the formulations used to calculate NDVI, FVC, LSE, albedo, LST and net radiation maps. Net radiation measured at the tower was compared with net radiation derived from the satellite both at the tower pixel and when averaged within the tower footprint. Sample maps of LST derived using the single channel algorithm are shown in Appendix A. Net radiation maps are shown in Appendix B.

Table 4.2: Total column water vapour estimates retrieved from ECMWF: http://apps.ecmwf.int/datasets/data/interim-full-daily/levtype=sfc/, and calculated AF's.

Date	Total column Water Vapour estimate [g/cm2]	φ_1 , φ_2 and φ_3
17/07/2013	1.5249	φ_1 1.07550
		φ_2 -0.33652
		φ_3 -0.17758
05/10/2013	1.5012	φ_1 1.07631
		φ_2 -0.32045
		φ_3 -0.20311
22/11/2013	2.009	φ_1 1.07465
		φ_2 -0.35496
		φ_3 -0.14901
24/12/2013	1.4607	φ_1 1.07675
		φ_2 -0.31238
		φ_3 -0.21618
25/01/2014	1.5734	φ_1 1.07697
		φ_2 -0.30838
		φ_3 -0.22271
26/02/2014	1.7065	φ_1 1.07750
		φ_2 -0.29915
		φ_3 -0.23796
30/03/2014	1.2977	φ_1 1.07471
		φ_2 -0.35354
		φ_3 -0.15119
17/05/2014	1.54046	φ_1 1.07560
		φ_2 -0.33449
		φ_3 -0.18077
02/06/2014	2.3522	φ_1 1.07369
		φ_2 -0.37807
		φ_3 -0.11425
04/07/2017	1.5399	φ_1 1.07646
		φ_2 -0.31766
		φ_3 -0.20761
21/08/2014	1.4263	φ_1 1.07562
		φ_2 -0.33403
		φ_3 -0.18149

4.8. Flux footprint

Flux footprint refers to the contribution of the upwind elements to fluxes measured at a point (Kim et al., 2006). Vesala et al. (2008) illustratively defines it as 'the field of view of the flux sensor'. An obvious cause of lack of energy balance closure as discussed by Wilson et al. (2002) is having the turbulent fluxes being measured from a different surface than that of the residual energy measurements. Knowing the turbulent fluxes source area can aid in understanding whether this is the case.

Over the past few decades, several footprint functions describing flux source areas have been developed. In this study, flux footprints were calculated using the Flux Footprint prediction (FFP) model by Kljun et al. (2015). FFP is a 2-dimensional parameterized footprint model, based on the 3-D backward Lagrangian stochastic particle dispersion model by Kljun, Rotach, & Schmid (2001). Unlike previous models, it makes it possible for evaluation of long time series data owing to its low computational demand. Apart from enabling calculation of single footprints, FFP allows calculation of climatology foot print from half hourly time step series. Aggregated climatology footprints were calculated for years 2012, 2013 and 2014. Single footprints were also derived during peak radiation at noon. For visualisation of extends on the study area, footprints were overlaid on a Google Earth image. The FFP MATLAB code used was downloaded from http://footprint.kljun.net/.

5. RESULTS AND DISCUSSION

5.1. Diurnal Variation of Fluxes

Figure 5.1 shows diurnal variations of flux partitions during the year 2012.

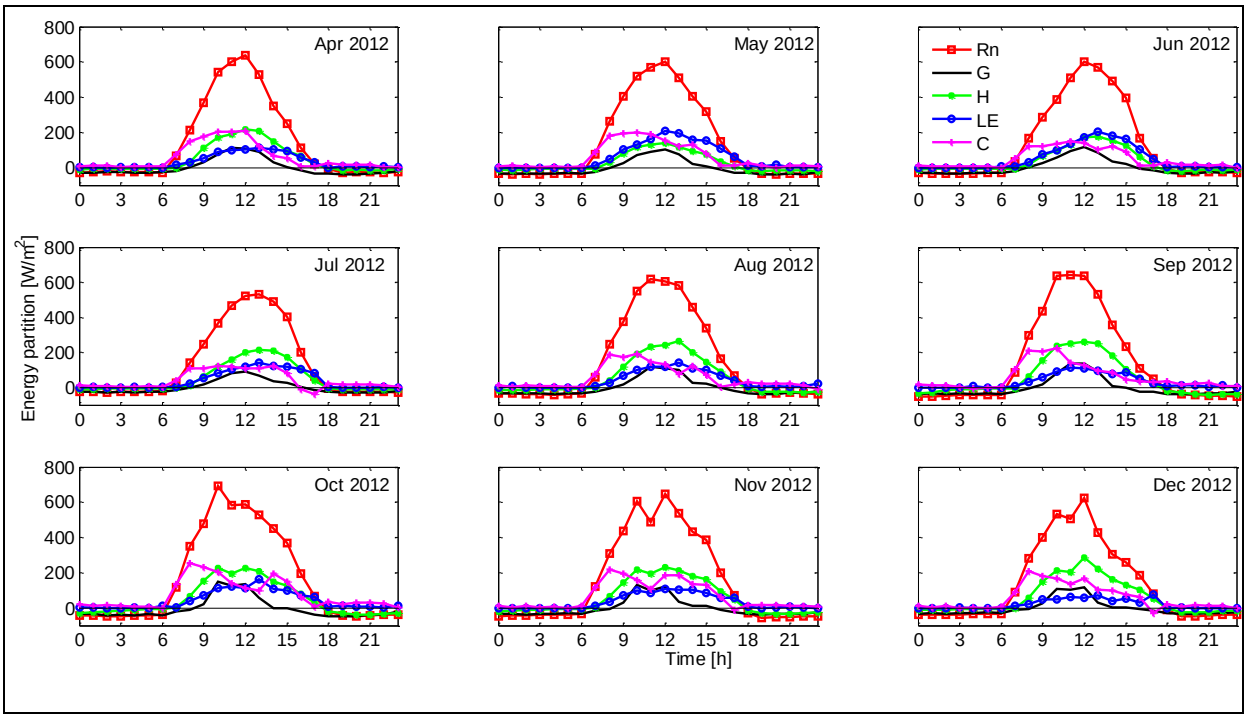

Figure 5.1: Hourly averaged fluxes showing diurnal flux variations in the year 2012. The closure term is shown in purple.

Net radiation peaks at 600-700 W m^{-2}, with slight variations over the months. As expected the peak occurs at midday. Sensible and latent heat show more variability; and even though sensible heat is generally higher than latent heat in most of the months, in May and June latent heat is higher than sensible heat. This is due to increased water availability following the rain season, thus increased evapotranspiration. After the rainy season, sensible heat becomes more dominant. Odongo et al. (2016) reported similar trends. Ground heat flux is the smallest of all fluxes and just as the sensible and latent heat, it peaks around midday, then gradually reduces over the evening, sometimes going to negative in the night. Table 5.1 shows a summary of monthly averaged energy partitions for the period between 2012 and 2014.

Table 5.1: Monthly averaged energy partitions for the period between 2012 and 2014. Closure term(C) is also shown

Year	Month	Rn [W/m-2]	G0 [W/m-2]	H [W/m-2]	LE [W/m-2]	C [W/m-2]	P [mm]
2012	Apr	141.10	0.50	45.80	31.89	62.91	6.08
	May	138.76	-4.50	39.90	34.41	68.95	3.78
	Jun	134.66	-0.14	40.91	37.47	56.41	0.62
	Jul	130.80	0.02	46.34	37.08	47.37	1.78
	Aug	153.41	0.10	53.11	32.81	67.39	2.83
	Sept	150.21	0.22	56.57	33.23	60.18	2.78
	Oct	167.76	0.13	50.26	32.22	85.16	4.18
	Nov	153.99	0.10	51.92	33.59	68.37	1.42
	Dec	139.71	0.14	53.84	24.64	61.08	2.18
2013	Jan	182.23	-0.76	50.40	33.08	99.51	3.34
	Feb	174.84	0.65	51.31	26.60	96.29	0.53
	March	157.42	0.42	51.53	26.59	78.89	6.4
	Apr	150.14	0.09	51.31	26.60	72.15	7.98
	May	157.51	0.07	51.27	26.59	79.58	1.67
	Jun	142.30	0.11	46.05	31.32	64.82	1.68
	Jul	154.68	0.03	56.25	23.55	74.85	2
	Aug	133.42	-0.46	51.10	18.71	64.07	3.13
	Sep	149.81	0.93	48.68	32.31	67.90	0.25
	Oct	172.42	0.13	54.38	21.45	96.46	0.96
	Nov	155.03	0.25	44.47	23.29	87.02	3.39
	Dec	148.57	-0.13	45.87	16.83	86.00	2.98
2014	Jan	176.62	0.38	67.26	20.16	88.82	1
	Feb	158.39	0.10	57.14	21.81	79.35	3.26
	March	192.66	0.27	56.13	27.50	108.76	0.81
	Apr	161.95	0.17	54.43	21.81	85.54	2.31
	May	141.58	0.24	53.99	22.74	64.60	1.27
	Jun	138.75	-0.07	53.96	19.52	65.34	1.61
	Jul	144.03	-0.39	56.18	27.51	60.73	3.12
	Aug	148.93	0.41	51.10	27.31	70.12	2.32
	Sept	165.89	0.03	48.11	25.33	92.42	3.08
	Oct	154.07	0.13	50.63	23.62	79.68	1.54
	Nov	138.60	-0.29	51.05	15.98	71.87	2.15
	Dec	157.45	-4.99	51.62	26.62	84.20	1.72

5.2. Energy Balance Closure

The energy balance ratio (EBR) analysed using data set filtered following Foken et al. (2004) was 67% for 2012, 56% for 2013 and 51% for 2014, with an overall EBR of 58% for the three year period (2012-2014). Slopes of linear regression of H+LE vs Rn-G were 0.72 for 2012, 0.60 for 2013 and 0.57 for 2014, with an overall slope of 0.63 for the three years as shown by the plots on Figure 5.2. The coefficient of determination (R^2) ranged between 0.63 and 0.78 while the RMSE ranged between 51.23 and 98.63 W m^{-2}. Energy balance closure analysis was also done for a brief period of 2016 (April 4th – June 3rd) when the sonic anemometer was working. The slope of linear regression for the 2 months evaluated in 2016 was 0.56, while the EBR was 0.49. The regression coefficients of H+LE vs Rn-G are summarized in Table 5.2.

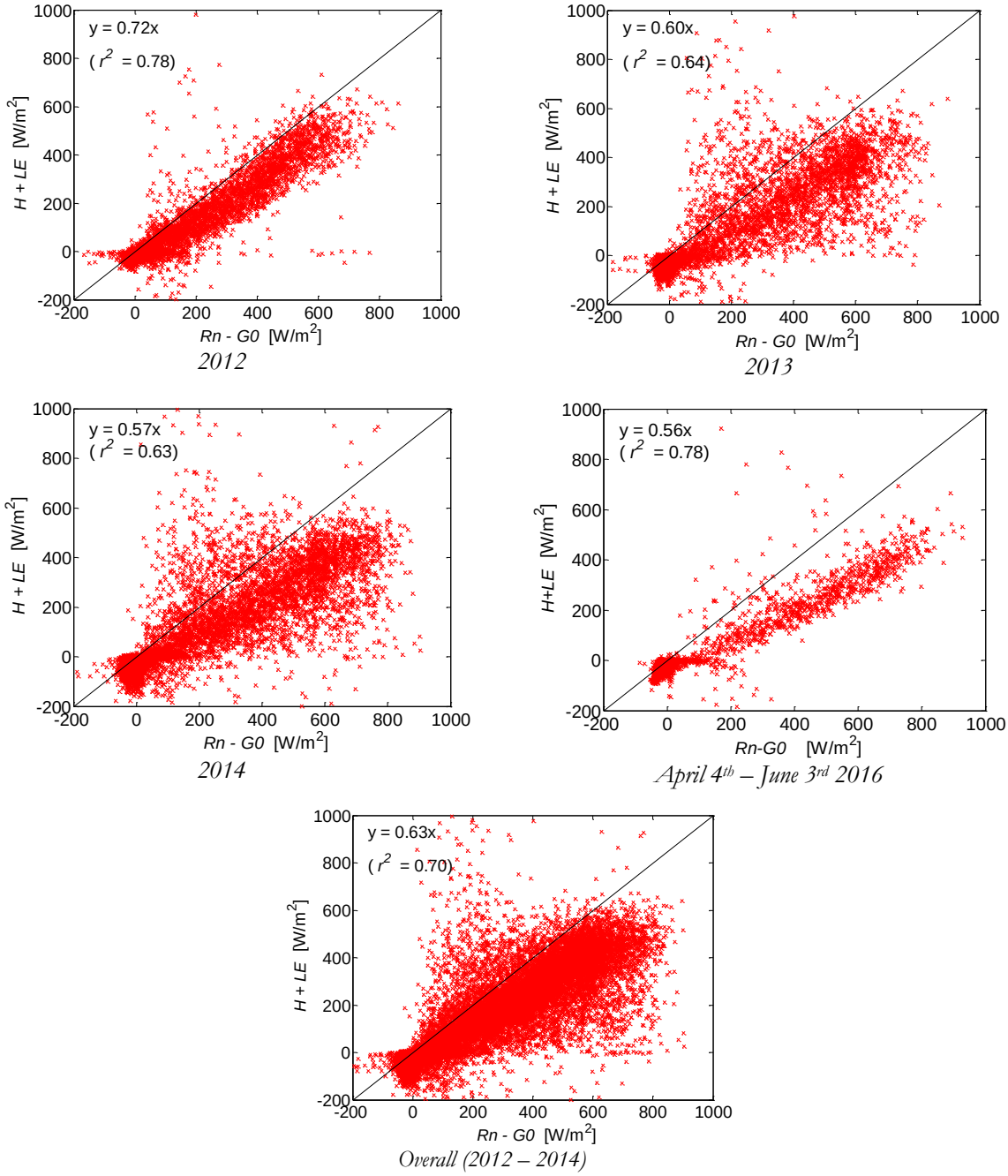

Figure 5.2: Linear regressions of Rn-G0 vs H+LE for 2012 – 2014 and April 4th – June 3rd 2016. Regression lines have been forced through the origin

Table 5.2: Summary of regression coefficients of Rn-G0 vs H+LE, EBRs and RMSEs for 2012 – 2014 and April 4th – June 3rd 2016

	Year	Slope	EBR	RMSE [W m^{-2}]	R^2
Original data set with Foken et al. (2004) quality flags	2012	0.73	0.67	51.23	0.83
	2013	0.60	0.56	98.63	0.64
	2014	0.57	0.51	94.01	0.63
	2016 (2 months)	0.56	0.49	61.10	0.78
	Overall (2012-2014)	0.63	0.58	85.61	0.70

It appeared that there was systematic reduction in EBR which reduced from 67% to 56%, 51% and 49% for 2012, 2013, 2014 and the two months evaluated in 2016 respectively. Slopes of linear regression of half hourly turbulent fluxes against the residual energy showed a similar reduction from 73% to 60%, 57% and 56% for 2012, 2013, 2014 and the two months evaluated in 2016 respectively. This could have been caused by drifts and systematic errors in the Bowen ratio measurement equipment.

5.2.1. Effect of Bowen Ratio Inter-calibration on Energy Balance closure.

Figure 5.3 shows a plot of linear regression of turbulent fluxes against the residual energy for the period between April 4th and June 3rd 2016 after the Bowen ratio inter-calibration.

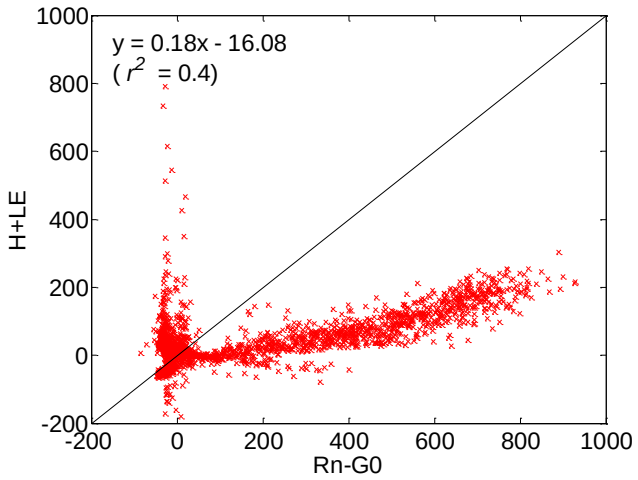

Figure 5.3: 2016 (April 4th-June 3rd) after Bowen ratio intercalibration

Inter-calibration did not improve the energy balance closure as it had been hypothesized. On the contrary, it deteriorated the closure to an unexpected value of 18% for measurements taken between April 4th and June 3rd 2016. A technical failure of the sensor aspirators during the inter-calibration period may have led to lack of reliable measurements.

5.2.2. Effects of Friction Velocity (u^* [ms^{-1}]) on the Energy Balance Closure

One of the conditions for the eddy covariance theory is fully developed turbulence. Low values of u^* [ms^{-1}] are associated with under-developed turbulence. Different authors have applied filtering of low quality data based on a friction velocity threshold (Barr et al., 2013; Nordbo et al., 2012). By filtering out fluxes when u^* was less than 0.25 m s^{-1}, Sánchez et al. (2010) reported an increase of 13% in the EBR. A filtering threshold of $u^* < 0.3$ m s^{-1} applied by Oliphant et al. (2004) was used in this study. After this filtering, the overall EBR for the three year period (2012-2014) improved by 5% while the yearly EBR's improved by 5% for 2012, 9% for 2013 and 5% 2014. The overall slope of linear regression improved by 3% while yearly slopes increased by 2% for 2012, 2% for 2013, and 4% for 2014. Closures obtained after applying this filtering were similar to those of Odongo et al. (2016) who reported an overall slope of 0.66 and an EBR of 0.65 for the three years. Table 5.3 summarises the results after filtering data when u^* was less than 0.3 m s^{-1}.

Table 5.3: Summary of Slopes of linear regression of Rn-G0 vs H+LE, EBRs and RMSEs after filtering fluxes when $u^* < 0.3$ m s^{-1}

	Year	Slope	EBR	RMSE [W m^{-2}]	R^2
Original data set with Foken et al. (2004) quality filters	2012	0.73	0.67	51.23	0.83
	2013	0.60	0.56	98.63	0.64
	2014	0.57	0.51	94.01	0.63
	2016 (2 months)	0.56	0.49	61.10	0.78
	Overall (2012-2014)	0.63	0.58	85.61	0.70
After filtering $u^* < 0.3$ m s^{-1}	2012	0.75	0.72	54.65	0.83
	2013	0.62	0.65	124.04	0.62
	2014	0.61	0.56	119.75	0.60
	2016 (2 months)	0.58	0.54	70.99	0.72
	Overall (2012-2014)	0.66	0.63	108.06	0.67

5.2.3. Effects of the Flux Footprint on the Energy Balance Closure

Flux footprint is defined as the contribution of the upwind elements to fluxes measured at a point. Figure 5.4 is a wind rose, showing the prevailing directions in the study area for the periods between 2012 and 2014.

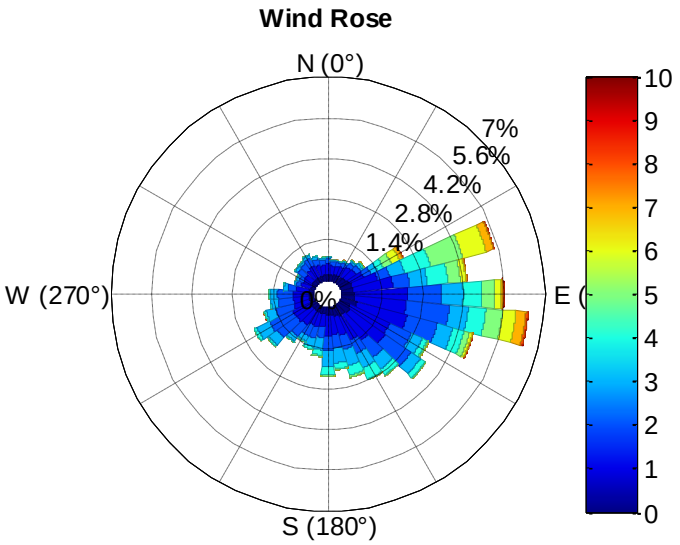

Figure 5.4: Rose diagram showing wind direction for period between 2012 and 2014. The colour bar indicates wind speeds (m s^{-1})

The prevailing wind direction is from from the ESE. Most average wind speeds were up to 5 m s^{-1} with a few instances of wind speeds above 6 m s^{-1}. Figure 5.5 and Figure 5.6 shows flux footprints derived using the FFP model.

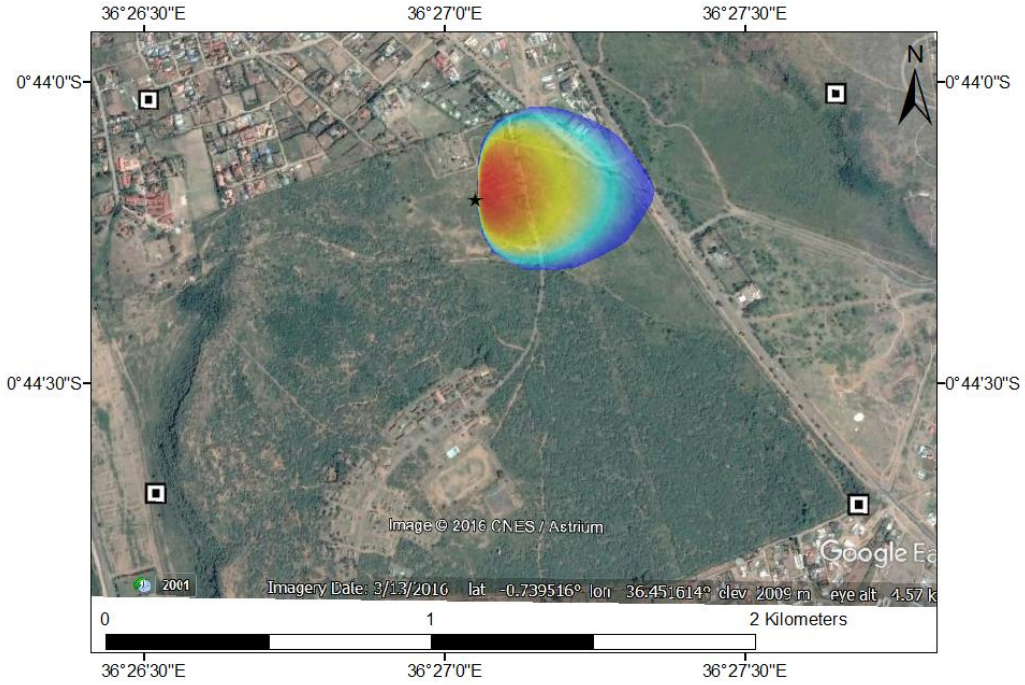

Figure 5.5: Midday flux footprint for 17/07/2013 overlaid on a true colour Google Earth image. The red intensity colour shows the highest contribution area, followed by the yellow, the cyan and the purple. The tower location is shown with a star.

During midday unstable condition (Figure 5.5), the footprint extends eastwards from the tower.

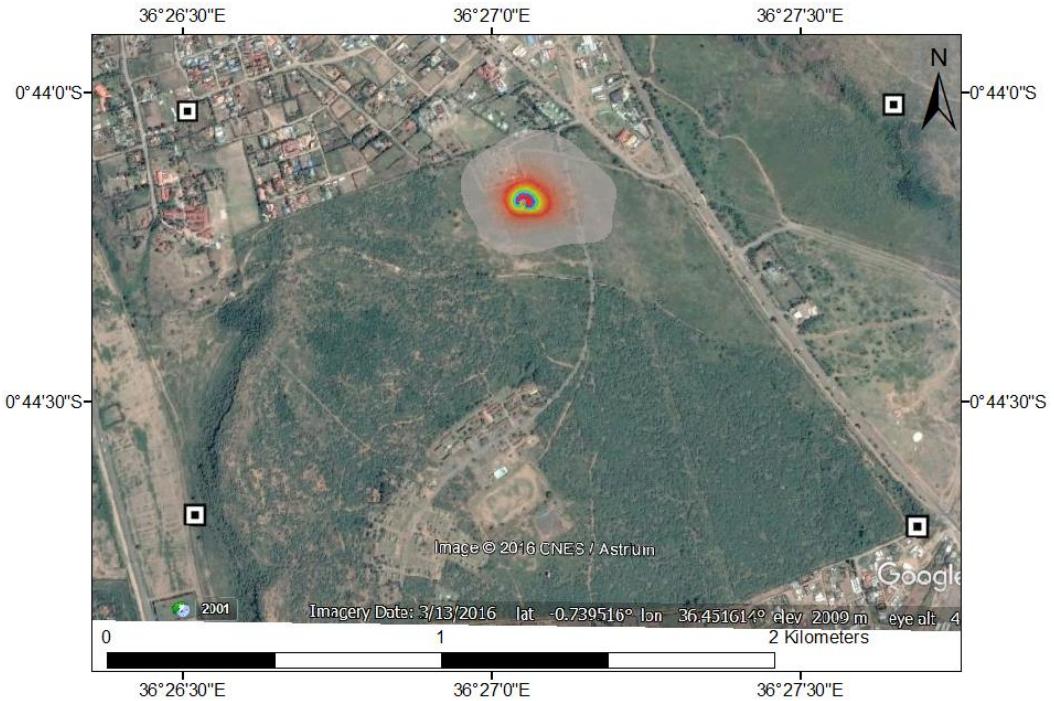

Figure 5.6: Three year climatology footprint (2012-2014). The middle high intensity colour represents highest contribution area. The contribution area reduces with decreasing colour intensity.

From the dimensions of the footprints, it is visible that most of the turbulent fluxes are from the same land cover as the residual fluxes. Some turbulent fluxes are however picked from across the road north eastwards of the tower location. Figure 5.7 shows polar plots of EBR with wind direction (*a*) as well as the footprint distance vs the wind direction (*b*).

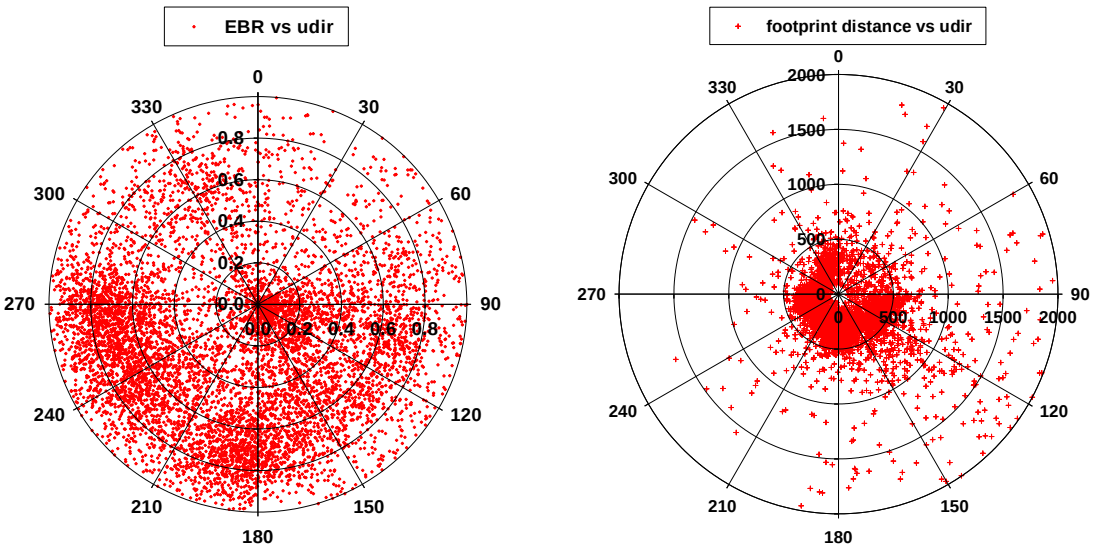

a) *b)*

Figure 5.7: Polar plot of EBR vs Wind direction for the period between 2012 and 2014.

Figure 5.7 b shows that most of the footprint source areas are within 500metres from the tower, with a few instances stretching beyond that especially when wind directions are between 60˚- 180˚. As seen in Figure 5.7 (*a)*, a higher concentration of low values of EBR are observed between 60˚- 150˚ degrees, and this could most likely be attributed to some fluxes emanating from the road surface to the East beyond the savannah in this quadrat. By filtering fluxes emanating from a bare land surface different from the forested area being investigated, Sánchez et al., (2010) found that EBR values improved by 5%. In this study fluxes when wind direction was between 60˚-150˚ were filtered, as they were considered to include the road surface. This increased the overall EBR for the three years (2012-2014) by 6% and yearly EBR's by 5%, 6% and 7% for 2012, 2013 and 2014 respectively. Table 5.4 summarises the coefficients of linear regression of Rn-G0 vs H+LE, the EBRs and RMSEs after filtering fluxes when wind direction was between 60˚ and 150˚.

Table 5.4: Summary of Slopes of linear regression, EBRs and RMSEs after filtering fluxes when wind direction was between 60˚ and 150˚

	Year	Slope	EBR	Mean Error [W m^{-2}]	R^2
Original data set with Foken et al. (2004) quality filters	2012	0.73	0.67	51.23	0.83
	2013	0.60	0.56	98.63	0.64
	2014	0.57	0.51	94.01	0.63
	2016 (2 months)	0.56	0.49	61.10	0.78
	Overall (2012-2014)	0.63	0.58	85.61	0.70
After filtering fluxes when wind direction was between 60˚- 120˚	2012	0.74	0.72	57.31	0.83
	2013	0.60	0.62	115.92	0.65
	2014	0.58	0.58	101.47	0.69
	2016 (2 months)	0.52	0.55	71.68	0.73
	Overall (2012-2014)	0.64	0.64	95.07	0.73

5.2.4. Accuracy in Ground Heat Flux Estimation.

Due to varying vegetation cover, topography and soil characteristics; representativeness of measured ground heat flux in heterogeneous areas becomes a challenge (Kustas et al., 2000). To obtain more representative measurements, many researchers use averaged measurements from two to nine soil heat flux plates (Stannard et al., 1994; Dugas et al., 1995). Stannard et al. (1994) reported an error of between 30 to 40 W m^{-2} in a semi-arid area while comparing measurements from different plates. While using a system of three sensors Kustas et al. (2000) reported deviations of up to 100 W m^{-2}. Figure 5.8 shows a plot of ground heat fluxes derived using the four additional soil heat flux plates installed during the fieldwork, together with ground heat flux derived from measurements by a plate to the South which has been taking measurements from 2012. Table 5.5 shows the standard deviation of Ground heat flux measurements from the four additional plates in comparison with the plate to the south

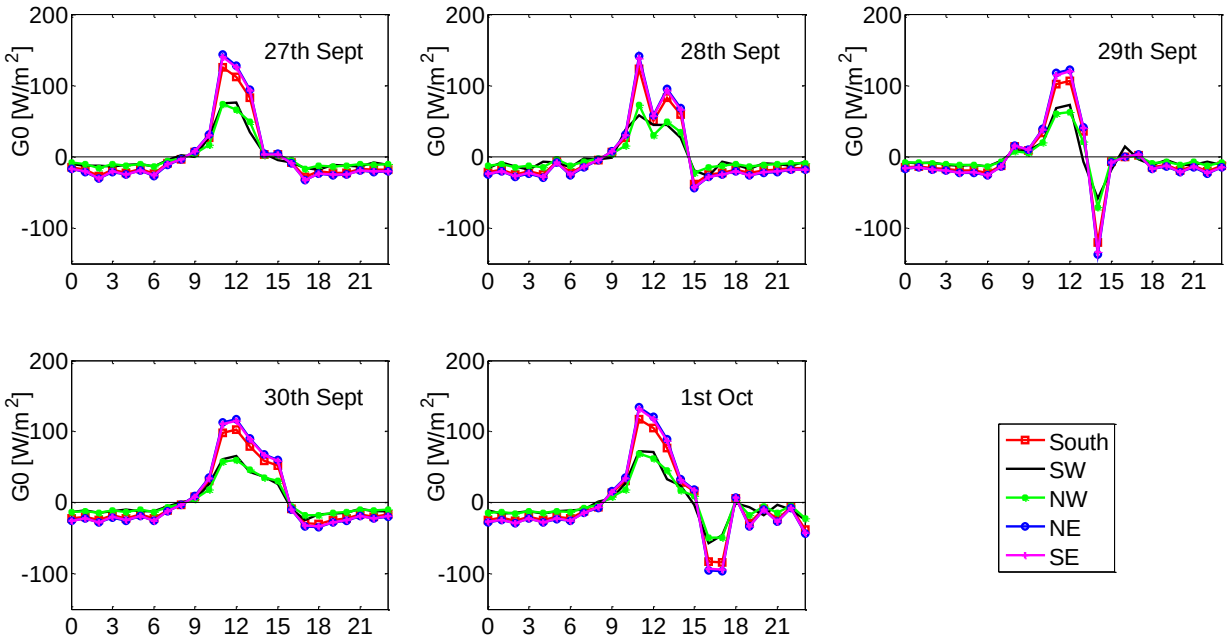

Figure 5.8: Comparison of G derived using measurements from soil heat flux plates installed in different directions (Note: South plate is at 10cm while all others are at 5cm)

Table 5.5: Standard deviation of Ground heat flux measurements from the four additional plates in comparison with the plate to the south.

	SE	NE	NW	SW
Standard Deviation (W m^{-2})	9.67	9.98	18.06	19.49

When compared to the south plate, ground heat fluxes derived from the west have a higher standard deviation than those from the east as shown in Table 5.5. Estimations from plates towards the west of the tower (SW and NW) show similarity, while those from the east and south of the tower show similarity as well. It should be noted that soil temperature profiles are only measured near the plate to the South and diffusivity estimated from these soil temperature profiles is assumed to be similar for all other directions. This assumption may not be correct, given that the soil thermal properties could be different for the different soil heat flux plate locations. Taking this into account, the variations could be different.

Considering the variability indicated by these measurements, there is a possibility of an error in ground heat flux when it is measured from one point and assumed to be representative of the whole area. Errors in estimation of ground heat flux can be up to 40% (Sánchez et al., 2010). Analysis of the energy balance closure using ground heat flux measurements in the different directions was not possible since the sonic anemometer was not working during the fieldwork period of this study.

5.2.5. Representativeness of Net Radiation Measurements and its Effect on Energy Balance Closure

As discussed in Section 3.1.3 , mismatch in footprint of net radiation and turbulent fluxes is a possible cause of lack of energy balance closure. Net radiation at the flux tower is measured by a net radiometer, mounted at 2.5 m above the ground. Compared to Landsat 8 OLI & TIRS satellite, the radiometer's field of view is relatively smaller in order of hundreds of m^{-2}. Figure 5.9 shows two sample maps of net radiation derived from Landsat 8.

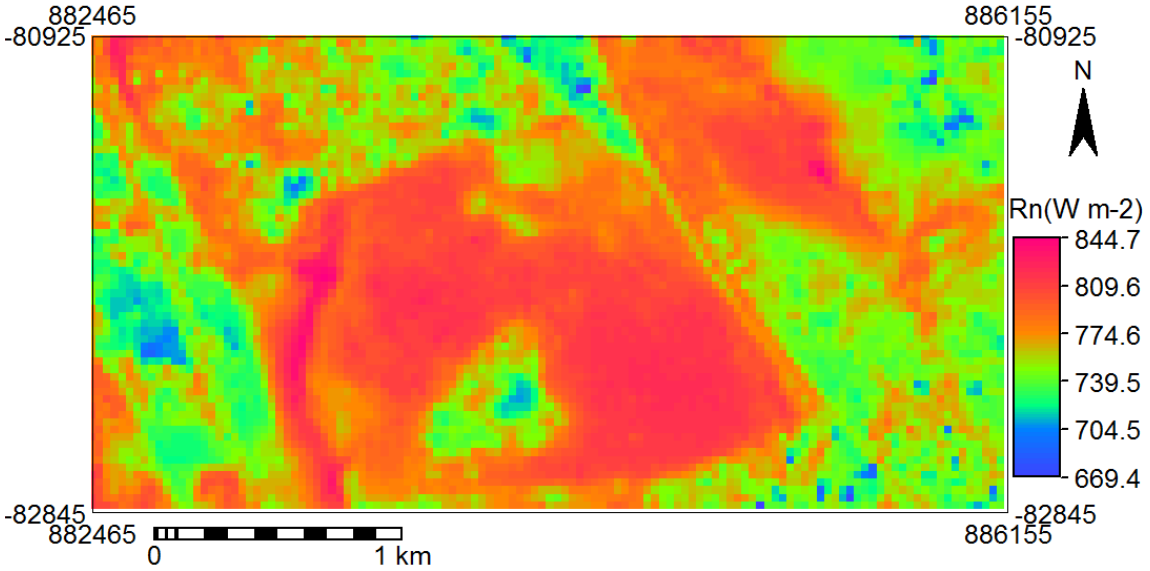

22/11/2013

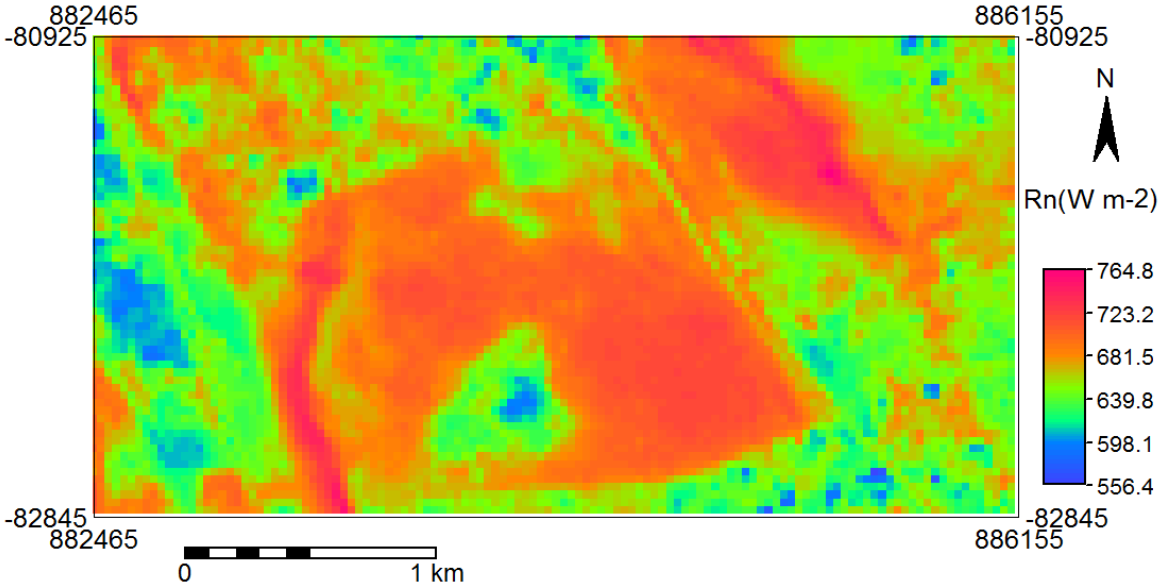

17/05/2014

Figure 5.9: Net radiation maps derived from Landsat 8 OLI & TIRS for 22/11/2013 and 17/05/2014. The maps show spatial variability in net radiation over the study area.

Net radiation varies spatially over the study area. As shown in Section 5.2.3, the turbulent fluxes source area (the tower footprint) extends up to several hundred metres from the tower. However, net radiation measured at the tower location is assumed to be equal to net radiation over the turbulent fluxes source area; which is not the case shown by the net radiation maps. Net radiation measured by the tower radiometer was compared with net radiation retrieved from Landsat 8 satellite images during 5 different overpass times when clear satellite images were available. In order to evaluate the representativeness, net radiation measured by the tower radiometer was compared with satellite retrieved net radiation aggregated over the tower footprint. Figure 5.10 shows the results of these comparisons.

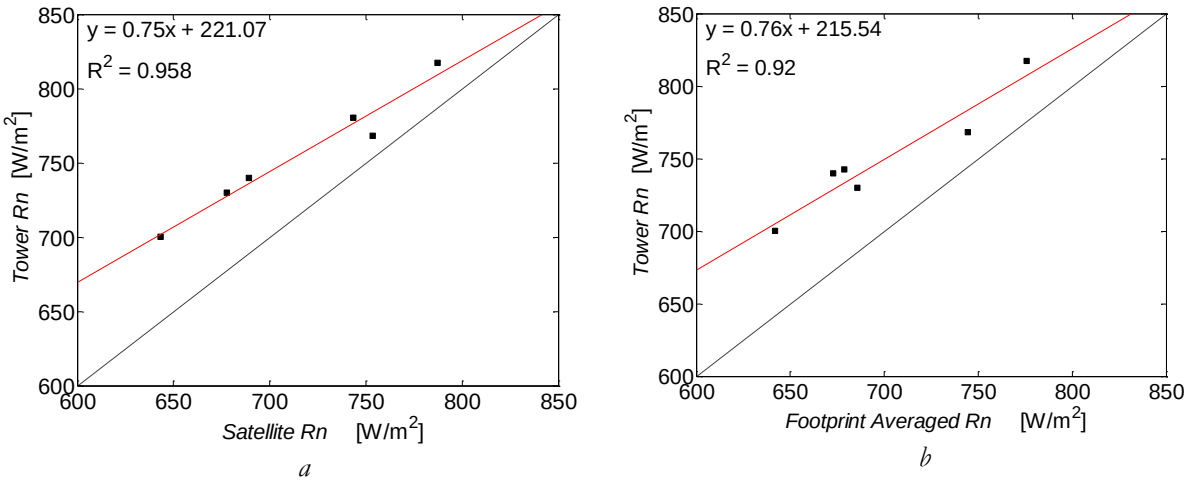

Figure 5.10: Comparisons of tower measured and satellite derived net radiation (Rn). (*a*) shows comparison with tower pixel value while (b) shows comparison with net radiation aggregated over the tower footprint area. The dashed line shows the 1:1 relationship.

Net radiation measured by the tower radiometer is higher than net radiation retrieved from the satellite with a mean error of ~50 W m-², both for the tower pixel value and when the satellite net radiation is averaged over the tower footprint. The coefficient of determination is 0.96 for comparison between satellite derived net radiation at the tower pixel and 0.92 for comparison with net radiation averaged within the tower footprint.

To account for the over-estimation when measurements are taken at a point by the tower radiometer, a bias correction factor was computed using the formulation in Eq. 5.1

$$\mathrm{BF} = \frac{\sum_{i=1}^{i=n} S}{\sum_{i=1}^{i=n} T} \qquad 5.1$$

Where BF is the bias factor, S refers to the satellite derived net radiation (averaged over the tower footprint), T is the tower measurements and n is the number of observations. The bias factor computed following this formulation was 0.93. Tower net radiometer measurements were corrected by multiplying them with this factor; and the effect of the correction on energy balance closure was evaluated. Applying this bias factor decreases the tower measured net radiation by ~5%. After correction of net radiation to account for the spatial variability, overall EBR increased by 5% for the three years (2012-2014), while individual EBRs for the years 2012, 2013, 2014 and the 2 months evaluated in 2016 increased by 11%, 4%, 12% and 7% respectively . Slopes of linear regression of H+LE vs Rn-G0 increased by 6% overall and yearly slopes increased by 5-7%. Table 5.6 shows a summary of coefficients of linear regression of H+LE vs Rn-G0 as well as EBRs after correcting for bias in net radiation.

Table 5.6: Summary of Coefficients of linear regression of H+LE vs Rn-G0, EBRs and RMSEs after correcting for bias in Rn

	Year	Slope	EBR	RMSE [W m^{-2}]	R^2
Original data set with Foken et al. (2004) quality flags	2012	0.73	0.67	51.23	0.83
	2013	0.60	0.56	98.63	0.64
	2014	0.57	0.51	94.01	0.63
	2016 (2 months)	0.56	0.49	61.10	0.78
	Overall (2012-2014)	0.63	0.58	85.61	0.70
Correcting for bias in Net Radiation	2012	0.80	0.78	58.87	0.82
	2013	0.65	0.60	99.13	0.63
	2014	0.63	0.63	101.93	0.68
	2016 (2 months)	0.60	0.56	71.82	0.73
	Overall (2012-2014)	0.69	0.63	86.31	0.69

5.2.6. Combining Friction Velocity filtering, Filtering when wind direction was between 60˚- 120˚ and Net Radiation Bias Correction.

When a combination of filtering data when $u^* < 0.3$ m s^{-1}, when wind direction is between 60˚- 120˚ and correcting for bias in net radiation is applied; the overall EBR for three years(2012 – 2014) becomes 76% which is an 18% increase from the original overall EBR of 58%. Yearly EBRs increased to 83%, 77%, 69% and 63% for 2012, 2013, 2014 and the 2 months of 2016 respectively. Despite being within closure values obtained by many authors in such areas, this closure is still low and other possible factors attributed to lack of closure that were not analysed in this study need to be evaluated. Figure 5.11 shows plots of linear regression of H+LE vs Rn-G after combined filtering.

Table 5.7: Summary of linear regressions coefficients, EBRs and RMSEs after combined filtering of data when $u^* < 0.3$ m s^{-1}, filtering when wind direction between 60˚- 120˚ and correcting for bias in net radiation

	Year	Slope	EBR	Mean Error (Wm^{-2})	R^2
Original data set with Foken et al. (2004) quality flags	2012	0.73	0.67	51.23	0.83
	2013	0.60	0.56	98.63	0.64
	2014	0.57	0.51	94.01	0.63
	2016 (2 months)	0.56	0.49	61.10	0.78
	Overall (2012-2014)	0.63	0.58	85.61	0.70
Combined filtering: $u^* < 0.3$ m s^{-1}, wind direction between 60˚- 120˚ and correcting for bias in net radiation	2012	0.83	0.83	60.81	0.86
	2013	0.71	0.77	149.24	0.69
	2014	0.66	0.69	127.11	0.67
	2016 (2 months)	0.61	0.63	63.05	0.71
	Overall (2012-2014)	0.74	0.76	114.73	0.74

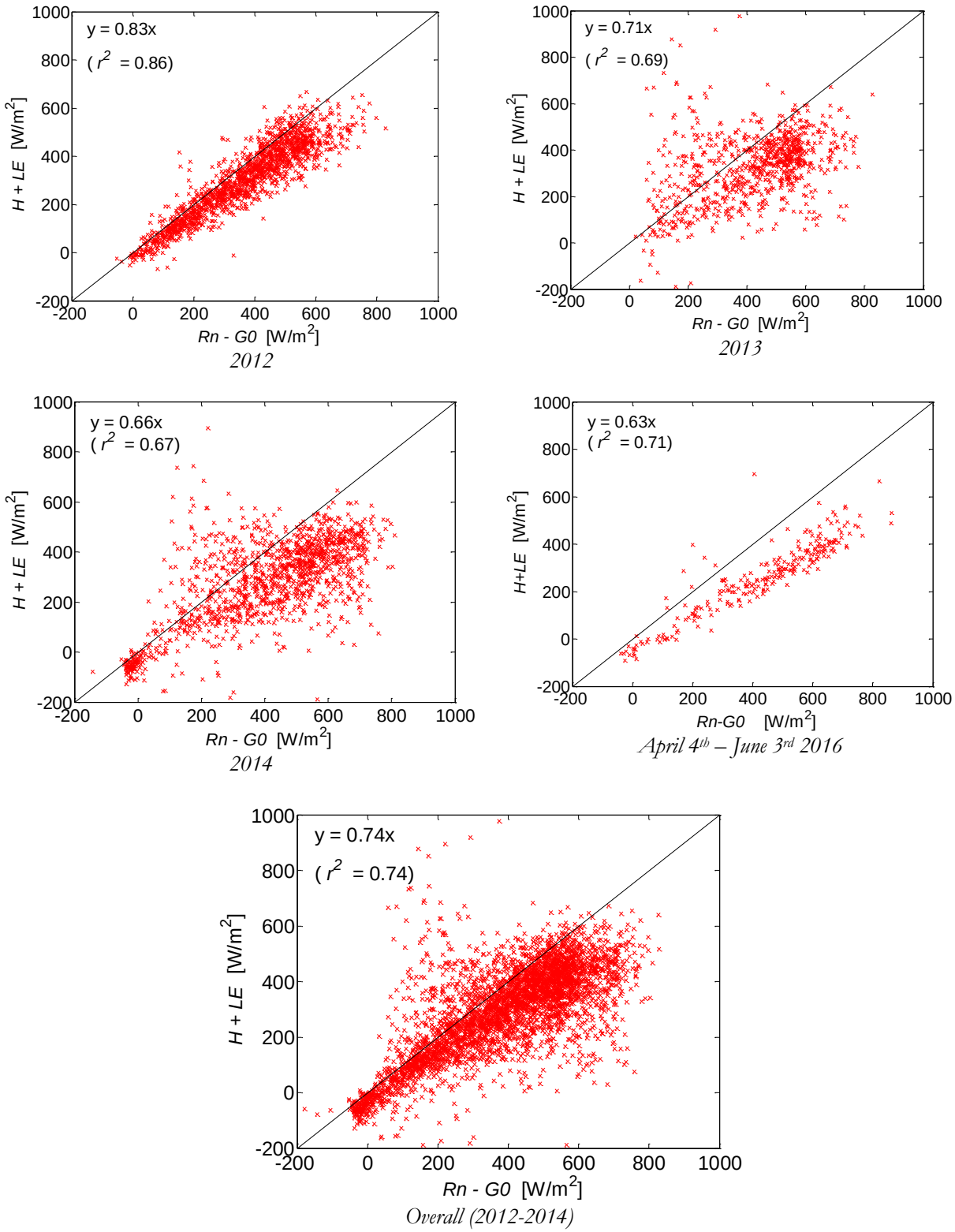

Figure 5.11: Linear regression of Rn-G0 against H+LE for the year 2012, 2013, 2014 and 2016 together with the three year overall 2012-2014; after combined filtering of data when $u^* < 0.3$ ms^{-1}, when wind direction is between 60°- 120° and correcting for the bias in net radiation. The regression lines have been forced through the origin.

5.2.7. Comparing Energy Balance Closure using Bowen Ratio Measurements and Gas Analyzer Measurements.

As aforementioned, the Naivasha flux tower relies on Bowen ratio measurements to derive latent heat flux. Standard eddy covariance systems use a gas analyzer which relies on the eddy covariance theory for direct measurements of latent heat. The disadvantage of Bowen ratio method is that it may not be able to capture small temperature and humidity gradients. Figure 5.12 shows comparison of latent heat flux derived using the Bowen ratio method with latent heat measured using a gas analyzer for the short period that the gas analyzer was installed in 2012.

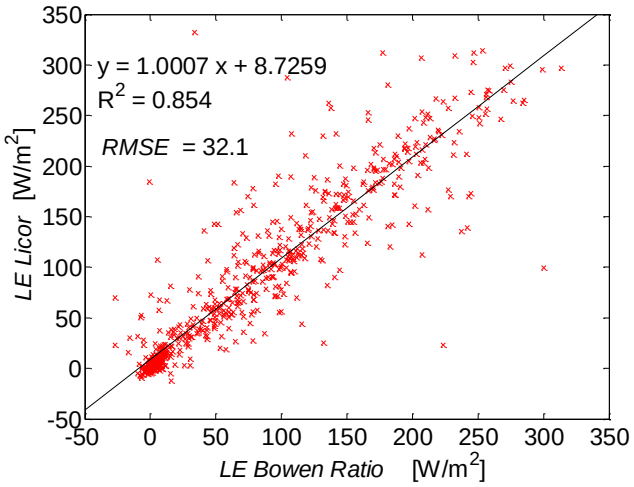

Figure 5.12 Comparison between Latent heat from Bowen ratio and latent heat measured by a gas analyzer for the days the gas analyzer was working

Latent heat measured using the gas analyzer is slightly higher than latent heat derived using Bowen ratio. The coefficient of determination (R^2) is 0.85, and the RMSE is 32.1. The Bowen ratio therefore under-estimates Latent heat flux for this site.

Energy balance closure was analyzed separately using LE measured with the gas analyzer and LE derived from Bowen ratio for the period when the gas analyzer operated. Figure 5.13 shows plots of linear regression of H+LE vs Rn-G0 using LE measured by gas analyzer and using LE derived from Bowen ratio.

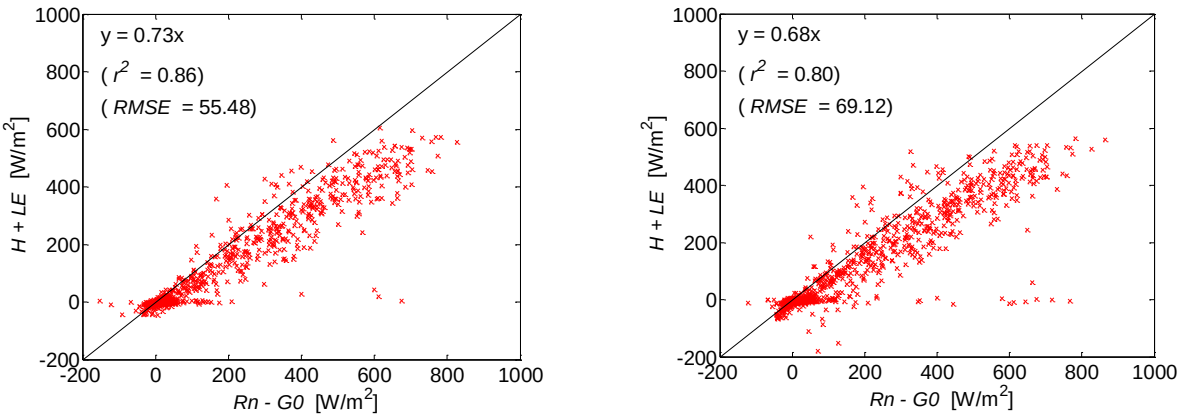

Using LE from gas analyzer *Using LE from Bowen ratio*

Figure 5.13: Linear regressions of H+LE vs Rn-G0 using LE measured by gas analyzer and using LE derived from Bowen ratio.

The EBR using LE measured by the gas analyzer was 77% compared to 66% when LE was derived using Bowen ratio for the same period. Slopes of linear regression gave closures of 73% using LE measured by the gas analyzer and 68% using LE derived from Bowen ratio. Figure 5.14 shows linear regressions of H+LE vs Rn-G0 after combined data filtering discussed in Section 5.2.6.

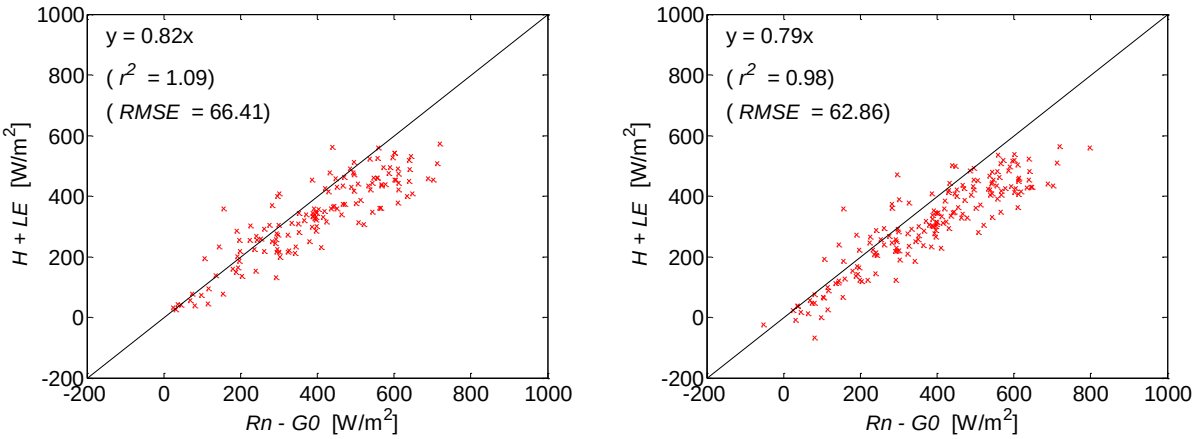

Using LE from gas analyzer *Using LE from Bowen ratio*

Figure 5.14: Linear regressions of H+LE vs Rn-G0 using LE measured by gas analyzer and using LE derived from Bowen ratio after combined data filtering discussed in Section 5.2.6

Using combined data filtering discussed in Section 5.2.6 improved the EBR calculated using LE measured by the gas analyzer to 84%, while EBR improved to 80% when using LE derived from Bowen ratio. The slopes show closures of 82% and 79% well within the EBR ranges.

6. CONCLUSION AND RECOMMENDATIONS

6.1. Conclusion

This research was mainly aimed at analyzing the causes of low energy balance closure using measurements taken from a flux tower situated in a semi-arid savannah area in Naivasha, Kenya.

The three year overall energy balance ratio (EBR) was 58% , while yearly closures were 67% for 2012, 56% for 2013, 51% for 2014 and 49% for 2 months analysed in 2016. Quality filtering of fluxes when u^* was less than 0.3 m s^{-1} improved the overall EBR for the three years evaluated by 5%. The flux footprint slightly extends into the nearby urban area towards the North and to the road surface towards the east of the tower. Filtering data containing fluxes from the road surface when wind direction is between 60˚-120˚, improved the EBR by 6%. Net radiation measured by the tower radiometer is higher than net radiation retrieved from Landsat 8 satellite both at the tower pixel and when averaged over the flux source area. Correcting for the bias in net radiation improved the overall EBR by 5%. Combining filtering data when $u^* < 0.3$ m s^{-1}, when wind direction is between 60˚- 120˚ and correcting for bias in net radiation improved the overall EBR for three years (2012 – 2014) to 76% which is an 18% increase. Yearly EBRs increased to 83%, 77%, 69% and 63% for 2012, 2013, 2014 and the 2 months of 2016 analyzed respectively. Despite being within closure values obtained by many authors in such areas, other possible factors attributed to lack of closure that were not analysed in this study need to be evaluated.

There is a systematic reduction in energy balance closures over the years which may be due to deterioration of Bowen ratio measuring equipment. Inter-calibration did not however improve the energy balance closure as it was expected. On the other hand, using a gas analyzer for latent heat flux measurements gives higher energy balance closures for the site than using Bowen ratio by.

There is a possibility of an error in estimation of ground heat flux due to lack of representativeness when only one soil heat flux plate is used to estimate ground heat flux.

6.2. Recommendations

1. Other factors attributed to lack of closure such as advection and averaging time that were not analysed in this study need to be evaluated.
2. A gas analyzer should be added to the tower for more accurate measurements of Latent heat fluxes.
3. For quantitative analysis of the effect of estimating ground heat fluxes using soil heat flux plate measurements in different directions on the energy balance closure, temperature profiles should be separately measured at each plate location, rather than relying on diffusivity estimated from only one location.

LIST OF REFERENCES

Aubinet, M., Grelle, A., Ibrom, A., Rannik, Ü., Moncrieff, J., Foken, T., … Vesala, T. (1999). Estimates of the Annual Net Carbon and Water Exchange of Forests: The EUROFLUX Methodology. *Advances in Ecological Research*, *30*(C), 113–175. http://doi.org/10.1016/S0065-2504(08)60018-5

Aubinet, M., Vesala, T., & Papale, D. (Eds.). (2012). *Eddy Covariance: A Practical Guide to Measurement and Data Analysis*. Springer. http://doi.org/10.1007/978-94-007-2351-1

Baldocchi, D., Falge, E., Gu, L., Olson, R., Hollinger, D., Running, S., … Hall, R. (2001). FLUXNET: A New Tool to Study the Temporal and Spatial Variability of Ecosystem-Scale Carbon Dioxide, Water Vapor, and Energy Flux Densities, *82*(11).

Barr, A. G., Richardson, A. D., Hollinger, D. Y., Papale, D., Arain, M. A., Black, T. A., … Schaeffer, K. (2013). Use of change-point detection for friction–velocity threshold evaluation in eddy-covariance studies, 171–172. http://doi.org/10.1016/j.agrformet.2012.11.023

Bowen, I. S. (1926). The Ratio of Heat Losses by Conduction and by Evaporation from any Water Surface. *Physical Review*, *27*(6), 779–787. http://doi.org/10.1103/PhysRev.27.779

Buck, A. L. (1981). New Equations for Computing Vapor Pressure and Enhancement Factor. *Journal of Applied Meteorology*. http://doi.org/10.1175/1520-0450(1981)020<1527:NEFCVP>2.0.CO;2

Clothier, B. E., Clawson, K. L., Pinter, P. J., Moran, M. S., Reginato, R. J., & Jackson, R. D. (1986). Estimation of soil heat flux from net radiation during the growth of alfalfa. *Agricultural and Forest Meteorology*, *37*(4), 319–329. http://doi.org/10.1016/0168-1923(86)90069-9

Dirmeyer, P. A. (1994). Vegetation Stress as a Feedback Mechanism in Midlatitude Drought. *Journal of Climate*, *7*(10), 1463–1483. http://doi.org/10.1175/1520-0442(1994)007<1463:VSAAFM>2.0.CO;2

Dragoni, D., Schmid, H. P., Grimmond, C. S. B., & Loescher, H. W. (2007). Uncertainty of annual net ecosystem productivity estimated using eddy covariance flux measurements. *Journal of Geophysical Research*, *112*(D17), D17102. http://doi.org/10.1029/2006JD008149

Dugas, W. A., Hicks, R. A., & Gibbens, R. P. (1995). Structure and function of C3 and C4 Chihuanhuan desert plant communities. Energy balancs components. *Journal of Arid Environments*.

Evans, J. G., McNeil, D. D., Finch, J. W., Murray, T., Harding, R. J., Ward, H. C., & Verhoef, A. (2012). Determination of turbulent heat fluxes using a large aperture scintillometer over undulating mixed agricultural terrain. *Agricultural and Forest Meteorology*, *166*, 221–233. http://doi.org/10.1016/j.agrformet.2012.07.010

Finnigan, J. J. (2004). A re-evaluation of long-term flux measurement techniques part II: Coordinate systems. *Boundary-Layer Meteorology*, *113*(1), 1–41. http://doi.org/10.1023/B:BOUN.0000037348.64252.45

Foken, T., Göckede, M., Mauder, M., Mahrt, L., Amiro, B., & Munger, W. (2004). POST-FIELD DATA QUALITY CONTROL. In X.lee et al (Ed.), *Handbook of Micrometeorology* (pp. 181–208). Kluwer Academic Publishers.

Foken, T., Wimmer, F., Mauder, M., Thomas, C., & Liebethal, C. (2006). Some aspects of the energy balance closure problem. *Atmos. Chem. Phys. Atmospheric Chemistry and Physics*, *6*, 4395–4402. Retrieved from www.atmos-chem-phys.net/6/4395/2006/

Goutorbe, J. P., Lebel, T., Dolman, A. J., Gash, J. H. C., Kabat, P., Kerr, Y. H., … Wallace, J. S. (1997). An overview of HAPEX-Sahel: a study in climate and desertification. *Journal of Hydrology*, *188–189*,

4–17. http://doi.org/10.1016/S0022-1694(96)03308-2

Heusinkveld, B. ., Jacobs, A. F. ., Holtslag, A. A. ., & Berkowicz, S. . (2004). Surface energy balance closure in an arid region: role of soil heat flux. *Agricultural and Forest Meteorology*, *122*(1), 21–37. http://doi.org/10.1016/j.agrformet.2003.09.005

Huxman, T. E., Wilcox, B. P., Breshears, D. D., Scott, R. L., Snyder, K. A., Small, E. E., … Jackson, R. B. (2005). ECOHYDROLOGICAL IMPLICATIONS OF WOODY PLANT ENCROACHMENT. *Ecology*, *86*(2), 308–319. http://doi.org/10.1890/03-0583

Jimenez-Munoz, J. C., Cristobal, J., Sobrino, J. A., Sòria, G., Ninyerola, M., & Pons, X. (2009). Revision of the single-channel algorithm for land surface temperature retrieval from landsat thermal-infrared data. *IEEE Transactions on Geoscience and Remote Sensing*, *47*(1), 339–349. http://doi.org/10.1109/TGRS.2008.2007125

Jiménez-Muñoz, J. C., & Sobrino, J. A. (2003). A generalized single-channel method for retrieving land surface temperature from remote sensing data. *J. Geophys. Res*, *108*(468810). http://doi.org/10.1029/2003JD003480

Jiménez-Muñoz, J. C., Sobrino, J. A., Plaza, A., Guanter, L., Moreno, J., & Martinez, P. (2009). Comparison Between Fractional Vegetation Cover Retrievals from Vegetation Indices and Spectral Mixture Analysis: Case Study of PROBA/CHRIS Data Over an Agricultural Area. *Sensors*, *9*(2), 768–793. http://doi.org/10.3390/s90200768

Kidston, J., Brümmer, C., Black, T. A., Morgenstern, K., Nesic, Z., McCaughey, J. H., & Barr, A. G. (2010). Energy balance closure using eddy covariance above two different land surfaces and implications for CO2 flux measurements. *Boundary-Layer Meteorology*, *136*(2), 193–218. http://doi.org/10.1007/s10546-010-9507-y

Kim, J., Lee, D., Hong, J., Kang, S., Kim, S. J., Moon, S. K., … Kim, S. (2006). HydroKorea and CarboKorea: Cross-scale studies of ecohydrology and biogeochemistry in a heterogeneous and complex forest catchment of Korea. *Ecological Research*, *21*(6), 881–889. http://doi.org/10.1007/s11284-006-0055-3

Kljun, N., Calanca, P., Rotach, M. W., & Schmid, H. P. (2015). A simple two-dimensional parameterisation for Flux Footprint Prediction (FFP). *Geoscientific Model Development*, *8*(11), 3695–3713. http://doi.org/10.5194/gmd-8-3695-2015

Kljun, N., Rotach, M. W., & Schmid, H. P. (2001). A Three-Dimensional Backward Lagrangian Footprint Model For A Wide Range Of Boundary-Layer Stratifications. *Boundary-Layer Meteorology*, *103*(2), 205–226. http://doi.org/10.1023/a:1014556300021

Kurc, S. A., & Small, E. E. (2004). Dynamics of evapotranspiration in semiarid grassland and shrubland ecosystems during the summer monsoon season, central New Mexico. *Water Resources Research*, *40*(9), n/a-n/a. http://doi.org/10.1029/2004WR003068

Kustas, W. P., Prueger, J. H., Hatfield, J. L., Ramalingam, K., & Hipps, L. E. (2000). Variability in soil heat flux from a mesquite dune site. *Agricultural and Forest Meteorology*, *103*(3), 249–264. http://doi.org/10.1016/S0168-1923(00)00131-3

Lee, X., & Hu, X. (2002). Forest-air fluxes of carbon, water and energy over non-flat terrain. *Boundary-Layer Meteorology*, *103*(2), 277–301. http://doi.org/10.1023/A:1014508928693

Liang, S., Shuey, C. J., Russ, A. L., Fang, H., Chen, M., Walthall, C. L., … Hunt, R. (2003). Narrowband to broadband conversions of land surface albedo: II. Validation. *Remote Sensing of Environment*, *84*(1), 25–41. http://doi.org/10.1016/S0034-4257(02)00068-8

Moncrieff, J., Valentini, R., Greco, S., Seufert, G., & Ciccioli, P. (1997). Trace gas exchange over terrestrial ecosystems: methods and perspectives in micrometeorology. *Journal of Experimental Botany*, *48*(310), 1133–1142.

Moore, C. J. (1986). Frequency response corrections for eddy correlation systems. *Boundary-Layer Meteorology*, *37*(1–2), 17–35. http://doi.org/10.1007/BF00122754

Nakai, T., Van Der Molen, M. K., Gash, J. H. C., & Kodama, Y. (2006). Correction of sonic anemometer angle of attack errors. *Agricultural and Forest Meteorology*, *136*(1–2), 19–30. http://doi.org/10.1016/j.agrformet.2006.01.006

Odongo, V. O., van der Tol, C., Becht, R., Hoedjes, J., Ghimire, C. P., & Su, Z. (2016). Energy partitioning and its controls over a heterogeneous semi-arid Shrubland Ecosystem in the Lake Naivasha Basin, Kenya. *Ecohydrology*. http://doi.org/10.1002/eco.1732

Ohmura Atsumu. (1982). Objective Criteria for Rejecting Data for Bowen ratio Flux calculations. *American Meterological Society*.

Oliphant, A. J., Grimmond, C. S. B., Zutter, H. N., Schmid, H. P., Su, H. B., Scott, S. L., … Ehman, J. (2004). Heat storage and energy balance fluxes for a temperate deciduous forest. *Agricultural and Forest Meteorology*, *126*(3–4), 185–201. http://doi.org/10.1016/j.agrformet.2004.07.003

Payero, J. O., Neale, C. M. U., Wright, J. L., Allen, R. G., Neale, C. M. U., & Allen, R. G. (2003). GUIDELINES FOR VALIDATING BOWEN RATIO DATA. *Transactions of the ASAE Journal Series NE*, *46*(69101), 1051–1060.

Redelsperger, J.-L., Thorncroft, C. D., Diedhiou, A., Lebel, T., Parker, D. J., Polcher, J., … Polcher, J. (2006). African Monsoon Multidisciplinary Analysis: An International Research Project and Field Campaign. *Bulletin of the American Meteorological Society*, *87*(12), 1739–1746. http://doi.org/10.1175/BAMS-87-12-1739

Sánchez, J. M., Caselles, V., & Rubio, E. M. (2010). Analysis of the energy balance closure over a FLUXNET boreal forest in Finland. *Earth Syst. Sci*, *145194*(10), 1487–1497. http://doi.org/10.5194/hess-14-1487-2010

Sobrino, J. A., Jiménez-Muñoz, J. C., Sòria, G., Romaguera, M., Guanter, L., Moreno, J., … Martínez, P. (2008). Land Surface Emissivity Retrieval From Different VNIR and TIR Sensors. *IEEE TRANSACTIONS ON GEOSCIENCE AND REMOTE SENSING*, *46*(2). http://doi.org/10.1109/TGRS.2007.904834

Song, C., Woodcock, C. E., Seto, K. C., Lenney, M. P., & Macomber, S. A. (2001). Classification and Change Detection Using Landsat TM Data: When and How to Correct Atmospheric Effects? *Remote Sensing of Environment*, *75*(2), 230–244. http://doi.org/10.1016/S0034-4257(00)00169-3

Stannard, D. I., Blanford, J. H., Kustas, W. P., Nichols, W. D., Amer, S. A., Schmugge, T. J., & Weltz, M. A. (1994). Interpretation of surface flux measurements in heterogeneous terrain during the Monsoon '90 experiment. *Water Resources Research*, *30*(5), 1227–1239. http://doi.org/10.1029/93WR03037

Tang, H., & Li, Z.-L. (2014). Radiometric Calibration in Thermal Infrared. In *Quantitative Remote Sensing in Thermal Infrared: Theory and applications* (p. 27). Heidelberg: Springer. http://doi.org/10.1007/978-3-642-42027-6

Tomlinson, B. S. a. (1996). Weighing-Lysimeter Evapotranspiration for Two Sparse-Canopy Sites in Eastern Washington.

Twine, T. E., Kustas, W. P., Norman, J. M., Cook, D. R., Houser, P. R., Meyers, T. P., … Wesely, M. L. (2000). Correcting eddy-covariance flux underestimates over a grassland. *Agricultural and Forest*

Meteorology, *103*, 279–300. Retrieved from http://digitalcommons.unl.edu/nasapub

USGS. (2015). Using the USGS Landsat 8 Product. Retrieved February 12, 2016, from http://landsat.usgs.gov/Landsat8_Using_Product.php

USGS. (2016). *LANDSAT 8 DATA USERS HANDBOOK* (Version 2.). USGS.

Van der Tol, C. (2012). Validation of remote sensing of bare soil ground heat flux. *Remote Sensing of Environment*, *121*, 275–286. http://doi.org/10.1016/j.rse.2012.02.009

Van der Tol, C., & Parodi, G. N. (2011). Guidelines for Remote Sensing of Evapotranspiration. *Evapotranspiration - Remote Sensing and Modeling*, 227–250. http://doi.org/10.5772/725

Vesala, T., Kljun, N., Rannik, Ü., Rinne, J., Sogachev, A., Markkanen, T., … Leclerc, M. Y. (2008). Flux and concentration footprint modelling: State of the art. *Environmental Pollution*, *152*(3), 653–666. http://doi.org/10.1016/j.envpol.2007.06.070

Vickers Dean & Mart, L. (1997). Quality Control and Flux Sampling Problems for Tower and Aircraft Data. *Journal of Atmospheric and Oceanic Technology*, 512–526. http://doi.org/10.1175/1520-0426(1997)014<0512:QCAFSP>2.0.CO;2

Vidale, P. L., Pielke, R. A., Steyaert, L. T., & Barr, A. (1997). Case study modeling of turbulent and mesoscale fluxes over the BOREAS region. *Journal of Geophysical Research*, *102*(D24), 29167. http://doi.org/10.1029/97JD02561

Wilson, K., Goldstein, A., Falge, E., Aubinet, M., Baldocchi, D., Berbigier, P., … Verma, S. (2002). Energy balance closure at FLUXNET sites. *Agricultural and Forest Meteorology*, *113*(1), 223–243. http://doi.org/10.1016/S0168-1923(02)00109-0

Yu, X., Guo, X., & Wu, Z. (2014). Land surface temperature retrieval from landsat 8 TIRS-comparison between radiative transfer equation-based method, split window algorithm and single channel method. *Remote Sensing*, *6*(10), 9829–9852. http://doi.org/10.3390/rs6109829

Zhang, G., Leclerc, M. Y., Duarte, H. F., Durden, D., Werth, D., Kurzeja, R., & Parker, M. (2014). Multi-scale decomposition of turbulent fluxes above a forest canopy. *Agricultural and Forest Meteorology*, *186*, 48–63. http://doi.org/10.1016/j.agrformet.2013.11.010

Appendix A. Land Surface Temperature Maps Derived Using the Single Channel Algorithm

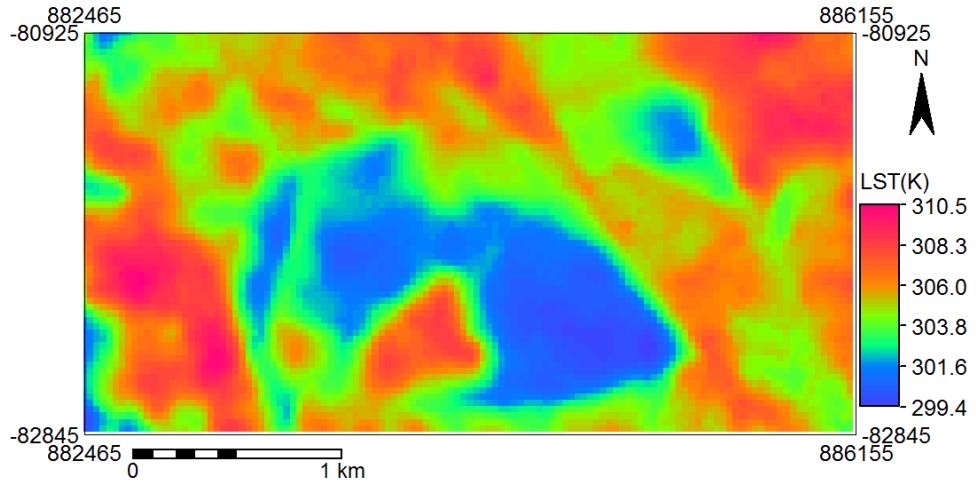

22/11/2013

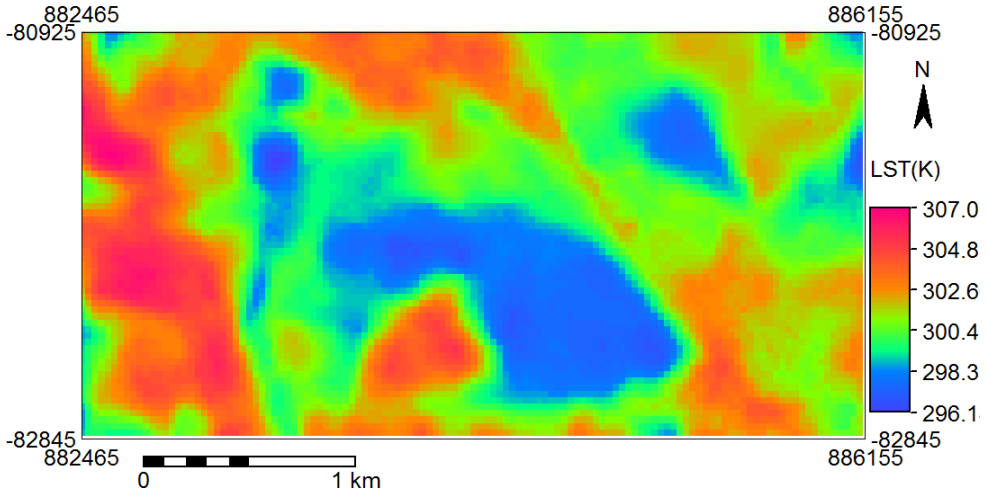

24/12/2013

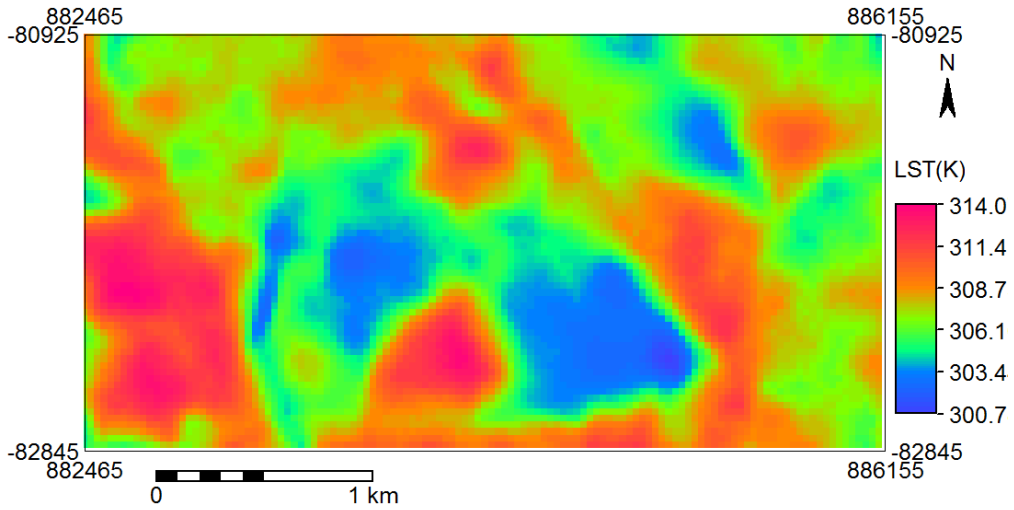

25/01/2014

Appendix B. Net Radiation Maps derived from Landsat 8 OLI & TIRS for the study area.

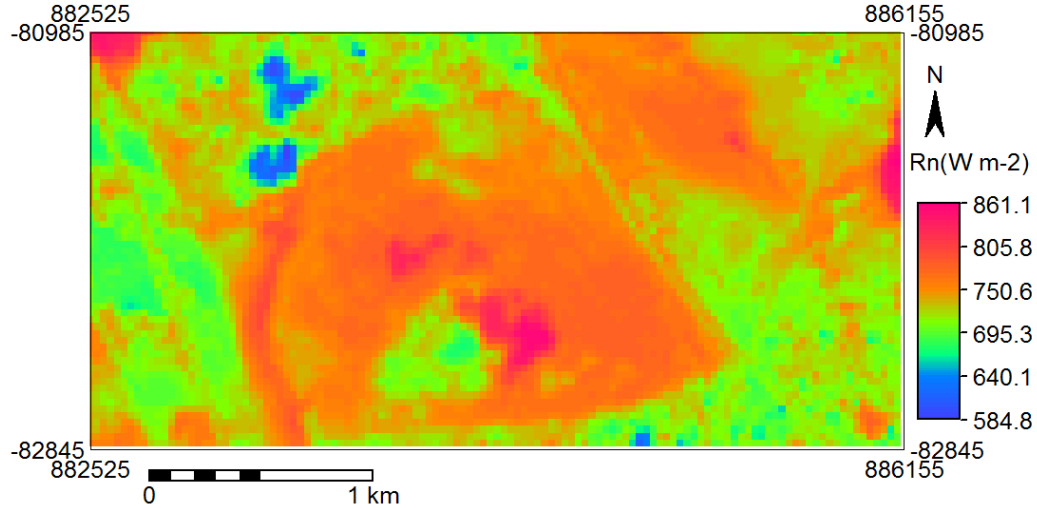

24/12/2013

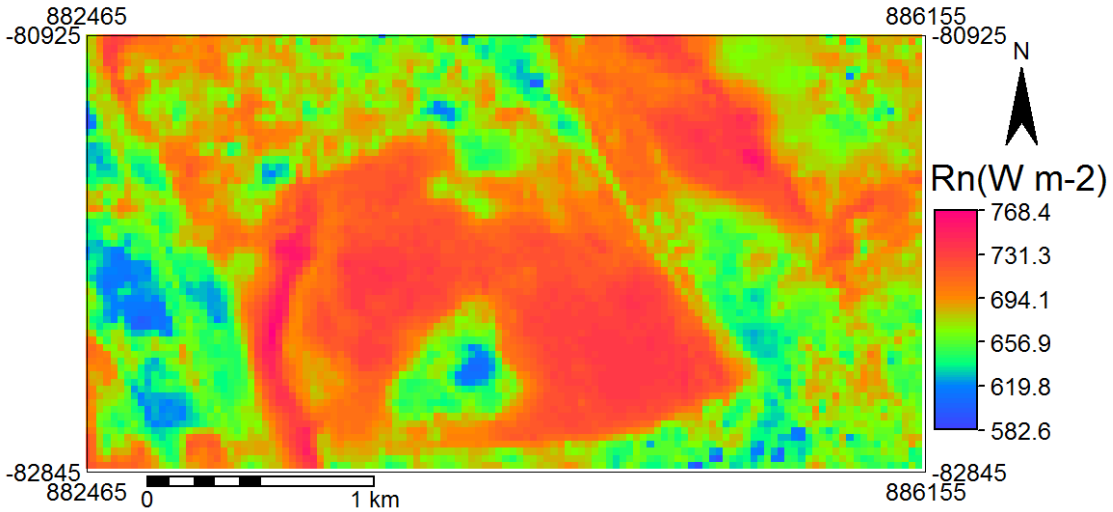

25/01/2014

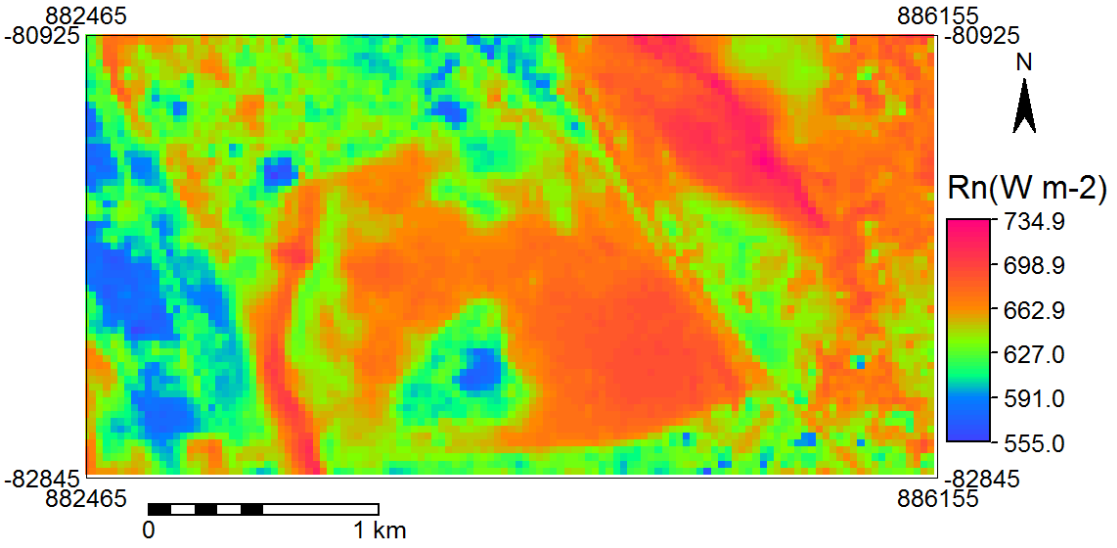

02/06/2014